

1 **Palaeozoic stromatoporoids and chaetetids analysed using Electron**  
2 **Backscatter Diffraction (EBSD); implications for original mineralogy and**  
3 **microstructure**

4  
5 Uwe Balthasar<sup>1</sup>, Stephen Kershaw<sup>2\*</sup>, Anne-Christine Da Silva<sup>3</sup>, Barbara Seuss<sup>4</sup>,  
6 Maggie Cusack<sup>5</sup>, Kilian Eichenseer<sup>1</sup>, Peter Chung<sup>6</sup>

7 1: School of Geographical, Earth and Environmental Sciences, Plymouth University,  
8 PL4 8AA, Plymouth; United Kingdom

9 2: Department of Life Sciences, Brunel University, Kingston Lane, Uxbridge, UB8  
10 3PH, United Kingdom

11 3: Sedimentary Petrology, Geological Departement, Liège University, Liège, 4000,  
12 Belgium

13 4: GeoZentrum Nordbayern (GZN), Paläoumwelt, Friedrich-Alexander University  
14 Erlangen-Nürnberg, Loewenichstraße 28, 91054 Erlangen, Germany

15 5: Division of Biological & Environmental Sciences, Faculty of Natural Sciences,  
16 University of Stirling, Stirling, FK9 4LA, UK

17 6: School of Geographical & Earth Science, University of Glasgow, Glasgow, G12  
18 8QQ, UK

19 \*Corresponding author; [Stephen.kershaw@brunel.ac.uk](mailto:Stephen.kershaw@brunel.ac.uk)

20  
21 **Abstract**

22 Palaeozoic hypercalcified sponges were ubiquitous Ordovician – Devonian reef  
23 builders but, despite their rich fossil record, their original skeletal mineralogy and  
24 microstructure remain poorly understood. This study provides the first application of  
25 electron backscatter diffraction (EBSD) to analyse skeletal structure of Silurian and  
26 Devonian stromatoporoids. The two Silurian and two Devonian stromatoporoid taxa  
27 selected are typical of stromatoporoids in showing poor preservation. A reference  
28 sample of an exceptionally well-preserved hypercalcified chaetetid sponge from the  
29 Carboniferous Buckhorn Asphalt Quarry (a fossil lagerstätte renowned for its  
30 preservation of skeletal microstructures) contains evidence that its skeleton  
31 comprised distinct bundles of single-crystal fibres, similar to modern hypercalcifying  
32 sponges. Similar bundles of crystal fibres are proposed here as the original  
33 microstructure of stromatoporoids, and acted as precursors to the coarse fibrous  
34 calcitic overprinting recrystallisation that is orientated normal to the growth layers,  
35 seen in all stromatoporoids viewed in cross-polarised light. The studied  
36 stromatoporoids show pronounced microporosity and micro-dolomite inclusions  
37 which are circumstantial evidence of an original composition of high-Mg calcite  
38 (HMC). We propose that the evidence of fibrous structures might be linked to  
39 inclusions of hydrated amorphous calcium carbonate (ACC·H<sub>2</sub>O) in the skeleton at  
40 the time of early diagenesis, as occurs in modern calcified sponges. The possible  
41 HMC skeletal composition of Palaeozoic stromatoporoids supports earlier views that  
42 the mineral composition of hypercalcifying reef builders is linked to Phanerozoic  
43 oscillations in the ratio of Mg:Ca, expressed as aragonite-calcite seas;  
44 stromatoporoids thrived in times of calcite-seas.

45 (239 words)

46  
47 **Key words:** stromatoporoid, chaetetid, sponges, micro-dolomite, high-magnesium  
48 calcite, aragonite-calcite seas

## 51 **Introduction and aims**

52 Sponges are intriguing for their ability to biomineralize a diverse range of minerals  
53 including aragonite, calcite, amorphous silica, and SiO<sub>2</sub>-CaCO<sub>3</sub> composite materials  
54 (Ehrlich et al. 2010, 2011; Gilis et al. 2011, 2013; Smith et al. 2013). Siliceous  
55 spicules are the most common mineralised structure in sponges and only about 8%  
56 of the ca. 8000 species of extant sponges secrete calcareous structures (Uriz, 2006);  
57 these calcifying sponges are generally restricted to cryptic reef environments (Gilis et  
58 al. 2013 and references therein). Calcareous mineralisation takes two forms: 1)  
59 calcitic spicules, normally considered to be the part of the primary sponge structure;  
60 and 2) massive calcitic or aragonitic basal skeletons that constitute a secondary  
61 structure in hypercalcifying sponges. Although calcareous spicules are a  
62 synapomorphy (present in ancestral forms and inherited by later forms, applicable in  
63 this case to modern forms) of the class Calcarea (Manuel et al. 2004; Voigt et al.  
64 2012), calcified basal skeletons are scattered among both calcareans and  
65 demosponges without any obvious phylogenetic significance (e.g. Voigt et al. 2012;  
66 Morrow & Cárdenas, 2015). Fewer than 20 genera of extant sponges are  
67 hypercalcifying (Smith et al. 2013), and none of them contribute significantly to  
68 modern-day reefs.

69 The present-day paucity of hypercalcified sponges and their minor role in reef  
70 systems is strongly contrasted by geological times when hypercalcified sponges  
71 were major reef builders (stromatoporoids during the Ordovician – Devonian) or reef  
72 components (chaetetids from the Devonian – Cretaceous and stromatoporoids  
73 during the Jurassic-Cretaceous) (Wood 1987; West 2012). However, despite their  
74 abundance in the fossil record, hypercalcified sponge calcification processes and  
75 original mineralogy are poorly understood because of pervasive recrystallisation that  
76 particularly affected stromatoporoids. Resolving this issue has application in two  
77 linked areas: 1) information on skeletal mineralogy will aid understanding of their  
78 biology of calcification; and thus, 2) the role of hypercalcified sponges in the debate  
79 regarding aragonite-calcite seas (Stanley & Hardie 1998). Therefore, the aim of this  
80 study is to advance understanding of skeletal structure and mineralogy of fossil  
81 hypercalcified sponges, using electron backscatter diffraction (EBSD), which, to our  
82 knowledge, has not been previously applied to these fossils. EBSD facilitates  
83 detailed analysis of crystal structure and orientation, not available by other means.  
84 The principal focus here is on Palaeozoic stromatoporoids because of their high-  
85 volume abundance in shallow-marine systems, and their long geological range  
86 (Middle Ordovician to Early Carboniferous, see Kershaw & Sendino 2020). However,  
87 available to the study is a well-preserved hypercalcified sponge chaetetid specimen  
88 from a Carboniferous Lagerstätte, that provides an important reference sample with  
89 which to compare middle Silurian and early Upper Devonian stromatoporoids, that is,  
90 time-periods when stromatoporoids left a rich fossil record. Because of the time-  
91 intensive process of EBSD study, we examine a limited number of specimens as a  
92 preliminary study to assess the viability of application of EBSD to this research area.  
93 We make inferences that may thus form the basis for more extensive study in future  
94 research.

## 95 96 97 **Literature background and relevance of original mineralogy of** 98 **stromatoporoids**

99 Stanley and Hardie (1998) set out a case that, throughout the Phanerozoic Eon, the  
100 fluctuation in the Mg:Ca ratio of seawater and its influence on the primary CaCO<sub>3</sub>

101 mineralogy had an important effect on the waxing and waning of the ecological  
102 importance of hypercalcified sponges. Those authors hypothesised that at times  
103 when Mg:Ca ratios were greater than two, aragonite precipitation was favoured  
104 ('aragonite seas'), whereas Mg:Ca ratios less than two favoured precipitation of  
105 calcite ('calcite seas') (see also Hardie 1996; Eichenseer et al. 2019). Stanley &  
106 Hardie (1998) argued that hypercalcified reef-building organisms are particularly  
107 susceptible to changes in aragonite-calcite sea conditions and that the type of  
108 skeletal mineralogy of dominant reef-builders coincides with either aragonite or  
109 calcite seas accordingly. With respect to sponges, they argued that the ecological  
110 dominance of Palaeozoic stromatoporoids is driven by the extensive calcite sea  
111 conditions that existed from the mid-Cambrian to the Early Carboniferous.

112 The interpretation of aragonite-calcite seas proposed by Stanley & Hardie  
113 (1998) relies on two key assumptions: (1) that among the multiple drivers of  
114 aragonite-calcite sea conditions, the Mg:Ca ratio is the main factor influencing the  
115 skeletal mineralogy of reef builders, and (2) that the original skeletal composition of  
116 fossil reef builders can be reliably determined. The first point has been challenged  
117 from the recognition by more recent work (Morse et al. 1997; Balthasar et al. 2011;  
118 Balthasar & Cusack 2015) which interprets CaCO<sub>3</sub> polymorph formation to have  
119 been driven by a combination of Mg:Ca ratio and temperature with the effect that,  
120 contrary to Stanley & Hardie (1998), warm shallow-water seas probably experienced  
121 aragonite-facilitating conditions throughout the Phanerozoic. However, recent work  
122 that combined Phanerozoic records of temperature and Mg:Ca ratios showed that  
123 even when corrected for the effect of temperature, aragonite-calcite sea conditions  
124 significantly relate to the ecological success of marine calcifiers throughout the  
125 Palaeozoic (Eichenseer et al. 2019).

126 The second assumption, the unambiguous identification of the original  
127 skeletal composition, is unresolved for Palaeozoic stromatoporoids, the dominant  
128 group of hypercalcified sponges in the fossil record. Although individual  
129 stromatoporoids often formed massive decimetre-sized skeletons that typically show  
130 a characteristic internal architecture of vertical and transverse skeletal elements (Fig.  
131 1), the reconstruction of primary skeletal composition is hampered by consistent  
132 recrystallization in the form of large irregular calcite crystals cutting across this  
133 internal architecture (Kershaw 2013). This type of preservation appears to be unique  
134 to stromatoporoids and presents a challenge to determine the primary skeletal  
135 composition. Although all Palaeozoic stromatoporoids are now calcite, their  
136 recrystallized nature has been interpreted by some authors as reflecting an original  
137 aragonitic skeleton (e.g. Semeniuk 1971; Stearn & Mah 1987; Mallamo & Stearn  
138 1991), supported by increased levels of strontium in a single spicule-bearing  
139 specimen (Da Silva et al. 2014). Other authors, however, have identified abundant  
140 micro-dolomite, which points to an original high-magnesium calcite (HMC)  
141 composition (e.g. Rush & Chafetz 1991; Yoo & Lee 1993). When considering that  
142 extant hypercalcified sponges construct their basal skeletons of aragonite, low-Mg  
143 calcite (LMC), or high-Mg calcite (HMC) (Smith et al. 2013), it is reasonable to  
144 expect that all these skeletal compositions were feasible for sponges at any time in  
145 the past. However, because stromatoporoids exhibit the same preservational style,  
146 described by Kershaw (2013), this is circumstantial evidence that they possessed  
147 the same original skeletal composition.

148 Reconstructing the original mineral composition of calcareous grains in  
149 limestone is challenging because, over geological time scales, aragonite is replaced  
150 by calcite; HMC either dissolves or loses its Mg content. Traditional means of

151 recognising an aragonite precursor of diagenetic calcite rely on elevated levels of  
152 strontium (e.g. Sandberg 1983) and HMC precursors are generally characterised by  
153 associated microdolomite (Dickson 2001a, b). Both these proxies are limited as they  
154 allow detection of the original mineralogy only if diagenesis occurred in a semi-  
155 closed system that retained the freed  $Mg^{2+}$  and  $Sr^{2+}$  ions. More recently, the  
156 application of electron backscatter diffraction (EBSD) to biomineralised and  
157 geological materials has opened up a new approach to questions of  
158 biomineralisation, palaeontology, and  $CaCO_3$  diagenesis (e.g. Cusack et al. 2008;  
159 Balthasar et al. 2011; Cusack 2016). EBSD provides information on the mineralogy  
160 and crystallographic orientation of individual grains with a potential submicronic  
161 resolution and thus can provide previously unavailable crucial information on the  
162 diagenetic history of rocks. Thus the application of EBSD provided here, to a variety  
163 of Palaeozoic stromatoporoids from various locations and a well-preserved chaetetid  
164 reference sample from the Pennsylvanian Buckhorn Asphalt Quarry (Oklahoma,  
165 USA), may help to explain the unique preservation of stromatoporoids, reconstruct  
166 the primary mineralogy of these sponges, and demonstrate striking similarities in the  
167 biomineralisation of Palaeozoic and modern hypercalcifying sponges.

168  
169

## 170 **Materials and Methods**

171 Stromatoporoid samples were carefully selected to examine similarities and  
172 differences using EBSD analysis. One sample of each of two Silurian stromatoporoid  
173 taxa, *Petridiostroma simplex* (Nestor) and *Pachystroma hesslandi* (Mori) were  
174 collected from the same limestone and marl facies of the lowermost Wenlock of  
175 Gotland, Sweden, chosen because the Silurian was a time of abundance of  
176 stromatoporoids, and also because the marly facies tend to leave better preserved  
177 specimens. These two taxa have very different skeletal architectures (Fig. 1, d-g)  
178 allowing comparison of different stromatoporoid taxa subjected to the same  
179 environmental and diagenetic conditions (Mori 1969). *P. simplex* is constructed of  
180 prominent continuous horizontal elements called laminae, separated by  
181 approximately circular vertical pillars, thereby enclosing a system of galleries filled  
182 with cement (Fig. 1 d, e). Galleries are interpreted to have been occupied by soft  
183 tissue in the upper few millimetres of living sponge, but below the living layer,  
184 galleries were empty and later filled with calcium carbonate cement, as in modern  
185 hypercalcified sponges. *P. hesslandi* is composed of a reticulate network of  
186 micropillars and microlaminae (Fig. 1 f, g), in which distinct laminae and pillars are  
187 not present, so that gallery space comprises small areas within the fine network.  
188 Thus *P. hesslandi* possesses a much finer structure than *P. simplex*; however, at  
189 hand specimen scale, growth layering is visible in both taxa (Fig. 1 a, b). Astrorhizae  
190 (canals in the skeleton that carried exhalant tubes of the sponge, Stearn 2015a) are  
191 common in *Pachystroma* (faintly visible in Fig. 1g) but rare in *Petridiostroma*, in  
192 which the exhalant tubes most likely lay in the soft-tissue layer above the skeleton,  
193 so did not leave evidence in the skeleton itself.

194 The two Devonian stromatoporoids are *Stictostroma* (two samples, Fig. 1h, i)  
195 and *Atelodictyon* (one sample, Fig. 1j, k), collected from the same locality in reef  
196 facies in middle Frasnian limestones of southern Belgium described by Da Silva et  
197 al. (2011a, b). *Stictostroma* and *Atelodictyon* are both constructed of well-defined  
198 laminae and pillars with prominent gallery space. *Atelodictyon* has blade-like pillars  
199 often joined forming chains (Fig. 1k) contrasting the separate circular pillars of  
200 *Stictostroma* (Fig. 1i).



201 At a finer scale of construction, stromatoporoids also possess microstructural  
202 variations within the laminae and pillars. The microstructure of *Petridiostroma*,  
203 *Pachystroma* and *Atelodictyon* is termed compact in stromatoporoid terminology  
204 (Stearn 2015b), and is micritic, different from *Stictostroma* which possesses a  
205 cellular microstructure. Unfortunately, because of operational problems, EBSD  
206 images were not obtained from *Stictostroma*, so its difference in microstructure could  
207 not be investigated. However, BSE and elemental maps of *Stictostroma* were  
208 assembled and compared with the other specimens.

209 The chaetetid from the Pennsylvanian (Upper Moscovian) Buckhorn Asphalt  
210 Quarry (Oklahoma, USA; specimen BSPG 2011 X 16 in Seuss et al. [2014]) was  
211 included because of its remarkable preservation. Chaetetid sponge skeletons,  
212 including the sample studied here, are characterised by elongate tubules that appear  
213 as polygonal honeycombs in cross section (Fig. 1, l-n), with walls of 50-100  $\mu\text{m}$  thick  
214 and a diameter of up to 500  $\mu\text{m}$  (Figs. 2, 3; see West 2012). Because sediments of  
215 the Buckhorn Asphalt Quarry were impregnated by hydrocarbons prior to or at the  
216 time of lithification, there is excellent preservation of calcareous shells, including  
217 aragonite (Seuss et al. 2009). Chaetetids and stromatoporoids were likely both  
218 originally composed of fibrous bundles of calcium carbonate crystals, as explained  
219 later. This chaetetid (Fig. 1, l-m) therefore provides a reference sample to compare  
220 with the stromatoporoids. Chaetetids are composed of a calcium carbonate fibrous  
221 structure that is normally very well preserved, in contrast to the recrystallised  
222 structure of stromatoporoids. A well-preserved stromatoporoid would have been  
223 ideal as a reference sample, but such does not seem to exist in the rock record. The  
224 detailed discussion of stromatoporoid mineralogy and diagenesis by Stearn (2015b)  
225 explores their variation, but recognition of original structures remains uncertain.  
226 Justification for the use of the Buckhorn chaetetid may be found from a series of  
227 papers by Gillis et al. (2011, 2012, 2013) who studied the skeletal microstructure of  
228 the basal skeleton of a diverse set of extant hypercalcifying sponges. They found  
229 that, independent of taxonomy or skeletal structure and mineralogy, almost all  
230 species investigated secrete their skeletons extracellularly and form single-crystal  
231 fibres and crystal bundles composed of up to 100 nm large grains. Thus, a detailed  
232 study using EBSD patterns of the chaetetid microstructure, as the best material  
233 available, to compare with microstructure of stromatoporoids, is a valuable approach  
234 to advance understanding.

235 The chaetetid specimen was treated initially with the organic solvent  
236 methylene chloride ( $\text{CH}_2\text{Cl}_2$ ) to remove asphalt from the specimen and then  
237 impregnated with araldite resin. Removal of the asphalt was important to avoid  
238 contamination of analytical instruments. The chaetetid and all stromatoporoid  
239 specimens were cut and polished down to 1 micron for backscatter scanning  
240 electron microscope (SEM) documentation. For EBSD analyses a FEI Quanta 200F  
241 field emission SEM equipped with an EDAX TSL Hikari high speed EBSD camera  
242 running Orientation Imaging Microscopy (OIM) software version 5.32 was used.  
243 Samples were highly polished (down to 0.06  $\mu\text{m}$ ) and coated with approximately 5  
244 nm of carbon, then analysed in high vacuum mode with a beam aperture of 50  $\mu\text{m}$   
245 and an accelerating voltage of 20 kV. The Kikuchi patterns were indexed using the  
246 American Mineralogist Crystal Structure (AMCS) database to identify the mineralogy  
247 and crystallographic orientation at each point in the EBSD map. EBSD images of two  
248 types are shown in this study: a) grey-scale diffraction intensity maps showing the  
249 intensity of diffraction at each point of the imaged area, an assessment of the image  
250 quality (IQ) of the EBSD data; and b) colour-coded crystal orientation maps (see Fig.

251 3e for the colour key for orientation of calcite crystals). Both types are illustrated in  
252 this study, together with some combined maps to compare the diffraction intensity  
253 with crystal orientation, thus aiding understanding of the nature of the skeletal tissue.

254 The PaleoReefs Database (PARED) was accessed on 20<sup>th</sup> April 2017. All  
255 Palaeozoic stromatoporoids and entries of chaetetid-grade sponges were treated as  
256 calcitic. The PARED entries were assigned to the 10 million-year time bins of the  
257 Paleobiology Database (see Alroy et al. 2008).

258

259

## 260 **Results**

261 The chaetetid reference has excellent preservation in terms of microstructure and  
262 composition and is therefore presented first. Its fibrous microstructure provides  
263 important evidence for interpretation of the stromatoporoid skeletal structures that  
264 also have evidence of a fibrous nature.

265

### 266 *Chaetetid microstructure*

267 The skeletal wall of the sample studied here is speckled with small irregular pores  
268 and has an overall grainy appearance in SEM backscatter images (Fig. 2b). The  
269 centre of the tubules is filled by blocky calcite cements that are often partially  
270 dissolved along cleavage planes (Fig. 2a). In the case of the Buckhorn sample  
271 studied here, the cement infill of the tubules and the skeletal wall is separated by a  
272 distinct gap that can reach tens of microns in thickness (Figs. 2-3); however,  
273 chaetetids normally lack this gap (e.g. Fig. 3a). Elemental maps (Fig. 2) show that  
274 this gap contains concentrations of carbon, which probably represent remaining  
275 traces of the asphalt that permeated the rock. This gap is also enriched in  
276 magnesium and contains many distinct crystals of dolomite that are juxtaposed to  
277 the skeletal wall (see also Fig. 6 in Seuss et al. [2014]) and likely formed before the  
278 asphalt migrated through the rock. Seuss et al. (2014) reported that most other  
279 chaetetid specimens from the same locality also contain earlier calcite cements that  
280 pre-date the asphalt emplacement.

281 EBSD analysis shows that the chaetetid skeletal wall is composed of distinct  
282 clusters of small calcite crystals that share similar, but not identical crystallographic  
283 orientations within each cluster (Fig. 3c-e). Clusters of crystallographically similar  
284 crystals are around 50-150 microns in dimension and share irregular boundaries.  
285 Individual crystals are blocky to elongate in cross section, 1-5  $\mu\text{m}$  wide, and fan out  
286 with the more blocky cross sections in the narrower parts of the clusters and the  
287 elongate cross sections in the wider parts (Fig. 3).

288

### 289 *Stromatoporoid microstructure*

290 All five stromatoporoid specimens investigated exhibit a prominent micro-porosity in  
291 their skeletal walls (Figs. 4-11). Pores vary from submicron to 8  $\mu\text{m}$  in size, are  
292 irregular to elongate in shape and seem randomly distributed (Figs. 4b; 5b; 8a). In  
293 addition to the pores, small inclusions are common that appear dark grey or bright  
294 grey/white in backscatter images (e.g. Fig. 8a). Elemental maps provide evidence  
295 that many of the darker crystals are Mg-rich (e.g. Fig. 8c), probably dolomite.  
296 Although the majority of dolomite is of submicron size and only evident through  
297 elemental maps, occasional clusters of larger (up to 10  $\mu\text{m}$ ) dolomite crystals occur  
298 in one specimen (Fig. 4b, d). Elemental maps also show little presence of Fe and Sr  
299 in stromatoporoids (Figs. 4, 6, 8, 9), discussed later.

300 EBSD analysis of the stromatoporoid samples shows that the porous skeletal  
301 walls are now composed of blocky calcite crystals that are syntaxially extended into  
302 the adjacent galleries (Figs 5b, 10c, 11). Two of the three stromatoporoids analysed  
303 with EBSD (*Pachystroma* and *Atelodictyon*) show that the part of the crystal  
304 representing the skeletal wall contains multiple regions with lattice defects in which  
305 the crystallographic orientation is slightly different from the neighbouring part of the  
306 same crystal (Figs 7c, 10c, 11c). In contrast, those parts of a crystal that extend  
307 beyond the skeletal wall into the gallery lack such defects and show a homogenous  
308 crystallographic orientation (most easily seen in Fig. 10c). The third specimen  
309 (*Petridiostroma*) analysed with EBSD shows no defects in either portion of the  
310 crystal, but shows clear syntaxial extension of the skeletal walls (Fig. 5b).

## 313 Discussion

314 This study addresses two linked aspects: 1) original microstructure, and original  
315 mineralogy, of the calcified sponge skeletons; and 2) the implications of the sponge  
316 skeletal features in the debate of aragonite-calcite seas. Although linked, these two  
317 aspects are considered separately, for clarity.

318 As a prelude to the discussion, we briefly discuss the terminology of high-Mg  
319 calcite (HMC). HMC is conventionally defined as calcite containing more than 4  
320 weight% Mg (e.g. Dickson 1991), but ultimately this threshold is arbitrary. The close  
321 association of dolomite with the skeletal walls of our stromatoporoid and chaetetid  
322 specimens leaves little doubt that the Mg contained in this dolomite was sourced  
323 from the skeletal walls. However, the concentration of Mg may not have exceeded  
324 the threshold of 4 weight%. So in this discussion we use the term HMC to indicate  
325 calcite that contained sufficient Mg to produce microdolomite inclusions, and LMC to  
326 indicate calcite that had such a low Mg content that microdolomite was not formed.

### 328 *Original microstructure*

329 The work of Gilis et al. (2011, 2012, 2013) on modern calcified sponges, noted  
330 earlier, provides an important link between modern and ancient representatives. The  
331 smallest building block of sponge skeletons has been interpreted to comprise  
332 submicronic grains of original amorphous calcium carbonate (ACC) (Gilis et al. 2013)  
333 composition. However, the *observed* fundamental crystallised unit consists of single  
334 crystals of only a few 100 nanometres width and several microns long, which are  
335 organised into larger bundles that grow from a single point (Gilis et al. 2013). Due to  
336 the fibrous crystal shape, neighbouring crystals fan out, growing away from the origin  
337 of the crystal bundle (Gilis et al. 2011, fig. 4; also our Fig. 12a). Because individual  
338 crystals can be expected to grow along the same crystallographic axes, each bundle  
339 should have a distinct crystallographic identity and sharp boundaries with  
340 neighbouring crystal bundles (Fig. 3c for chaetetid, see also model drawing in Fig.  
341 12a,b). This model can be applied to a variety of extant taxa from both Calcarea and  
342 Demospongia and it is likely to represent a plesiomorphic (i.e. ancestral) character  
343 for skeletal secretion; it is thus used as a working hypothesis for the secretion of the  
344 Palaeozoic chaetetid and stromatoporoids investigated here. The only noticeable  
345 exception to an extracellular assemblage of crystal fibres is the modern demosponge  
346 *Astrosclera willeyana*, which uses digested bacterial remains to seed aragonite  
347 spherules that grow intracellularly (Jackson et al. 2010; Wörheide 1998). However,  
348 the unusual skeletal secretion of *A. willeyana* is interpreted to have been acquired by  
349 horizontal gene transfer from associated bacteria (Jackson et al. 2011) and is

350 unlikely to reflect a shared biomineralisation pathway for a larger taxonomic group of  
351 sponges.

352 The crystal fan model outlined above is consistent with the microstructure of  
353 the Buckhorn chaetetid (Fig. 3b-e), which shows distinct clusters of crystals with  
354 similar crystallographic orientation and shapes that can easily be visualised as a  
355 horizontal to oblique cross section through a fan of single-crystal fibres. However,  
356 with up to 5  $\mu\text{m}$  in size, individual crystals in the chaetetid skeletal walls are much  
357 bigger and more irregular than those from extant sponges (Gilis et al. 2011, 2012,  
358 2013). This difference can be attributed to the transformation from diagenetically  
359 unstable HMC to stable LMC via a micron-scale dissolution-precipitation process  
360 because the altered structure retains a fibrous character interpreted to reflect the  
361 pre-alteration crystal bundles. By comparison, in echinoderms, this process can  
362 preserve micron-scale microstructures while at the same time preserving micro-  
363 porosity and micro-dolomite within the space of the primary skeleton (Dickson  
364 2001a, b). In echinoderms, the best preservation was observed when the stereom  
365 was filled by low magnesium ferroan calcite (Dickson 2004), evidence that  
366 entombment within stable low-magnesium calcite protected the less stable HMC of  
367 the echinoderm skeleton from diagenetic pore fluids. We interpret the asphalt  
368 impregnation of the Buckhorn chaetetid has effectively resulted in the same  
369 protection, because the apparent dissolution of calcite cement within the tubules has  
370 not noticeably affected the skeletal walls in the studied specimen.

371 For the stromatoporoids, their diagenesis resulted in coarse blocky calcite  
372 crystals with lattice defects. The defects are clearly constrained to the skeletal  
373 portion of crystals of those two taxa, whereas crystallographically homogenous  
374 regions occupy non-skeletal areas (i.e. galleries) of the structure. Presence of  
375 subcrystals with varying orientations in the skeletal parts of *Pachystroma* and  
376 *Atelodictyon* (Figs. 7, 10 and 11) are thus interpreted as diagenetic fusions and  
377 alteration of multiple individual crystals that originally had similar, but not identical  
378 crystallographic orientations. In diagenetic terms, single crystals with multiple internal  
379 crystallographic alignments are unstable and we interpret that they became  
380 crystallographically homogenous structures over time. However, there are some  
381 differences in the structure of the stromatoporoids. The specimen of *Petridiostroma*  
382 (Fig. 5) does not show the subtle variations in subcrystal orientations preserved in  
383 *Pachystroma* and *Atelodictyon*, for which we consider two possible interpretations: a)  
384 variations in diagenetic history between stromatoporoids; or b) [more likely]  
385 *Petridiostroma* was constructed differently from the other two taxa and lacked  
386 bundles of small crystals when it grew. *Petridiostroma* and *Pachystroma* occur  
387 together, sometimes in the same stromatoporoid specimen, where one overgrew the  
388 other, and were presumably affected by the same diagenetic processes. Although  
389 Stearn (2015b) noted that variation of stromatoporoid microstructure may relate to  
390 different processes of alteration, we consider a more likely scenario is that the  
391 diagenetic pathways were the same, but differing original structure of the  
392 stromatoporoid influenced the diagenetic result. These preliminary interpretations will  
393 require a larger sample of different taxa to investigate using EBSD. In *Pachystroma*  
394 and *Atelodictyon*, the shape and size of calcite crystals with domains of  
395 crystallographic misalignments in the stromatoporoid skeletal walls are very similar  
396 to the crystal bundles described for chaetetids above. We therefore view this  
397 similarity as evidence that the same principal biomineralisation sequence applies, i.e.  
398 based on the Gilis et al. (2011) model discussed above (also Fig. 12).

399

400 *Original mineralogy*

401 Diagenesis of echinoderm skeletons provides a valuable model for the recognition of  
402 original HMC composition in fossil skeletal material, outlined here for comparison  
403 with stromatoporoids. Experimental studies have shown that when heated up to 300°  
404 C, with and without added water, echinoid plates of HMC composition transform to  
405 calcite + dolomite together with a characteristic micro-porosity (Dickson 2001a).  
406 Importantly, these heating experiments showed that dolomite formation is a  
407 dissolution-precipitation process that depends on the availability of intra-skeletal  
408 water. The irregular distribution of the experimentally produced micropores is thus  
409 controlled by the distribution of water within the skeletal calcite. Molecular water is  
410 found in many calcifying organisms (Gaffey 1988), and in echinoderm skeletal plates  
411 it can make up to 3.38% of their weight (Gaffey 1995). The presence of water within  
412 calcareous skeletons is most likely linked to hydrated amorphous calcium carbonate  
413 (ACC·H<sub>2</sub>O) which in echinoderms forms the initial precursor of HMC (Politi et al.  
414 2004). Although ACC·H<sub>2</sub>O transforms via ACC to HMC in a matter of hours,  
415 nanometric traces of ACC·H<sub>2</sub>O can survive within the mature calcite structure,  
416 probably due to stabilisation by proteins (Gong et al. 2012). Following this argument,  
417 the stability of ACC·H<sub>2</sub>O within skeletal structures should be dependent on the  
418 stability of the relevant proteins. Although intra-skeletal proteins might not be stable  
419 over longer geological time scales (Marin et al. 2014), the preservation of such  
420 proteins in 1500-year old snails (Sarashina et al. 2008) is evidence that the water  
421 associated with skeletal ACC·H<sub>2</sub>O becomes available in the course of early  
422 diagenesis. A critical point is that because fossil echinoderms from non-  
423 metamorphosed sedimentary rocks exhibit the same pattern of microporosity and  
424 dolomite as produced in experiments on modern echinoderms (Dickson 2001b), it is  
425 reasonable to interpret that the diagenetic pathways described are not dependent on  
426 excessive heating.

427 From the above discussion, diagenesis of the Buckhorn chaetetid and  
428 stromatoporoids is consistent with the presence of ACC·H<sub>2</sub>O in their original  
429 mineralised skeleton. A role of ACC in skeletal secretion has so far been  
430 documented for only the calcite spicule formation of the calcarean genus *Clathrina*  
431 (Aizenberg et al. 1996; Sethmann & Wörheide 2008), but has also been interpreted  
432 to play a role in the formation of the basal skeletons of hypercalcifying sponges (Gillis  
433 et al. 2013), although direct evidence is still missing. In summary, the distinct  
434 preservation of the fossil sponges is consistent with a role of ACC·H<sub>2</sub>O in the  
435 biomineralisation of Palaeozoic stromatoporoids and the Buckhorn chaetetid (Fig.  
436 12).

437 Because both echinoderms and stromatoporoids retain evidence of primary  
438 structure in their altered states in fossil material, we interpret this comparability as  
439 evidence that crinoids found in the same samples as sponges investigated here  
440 were affected by the same diagenetic conditions. Both the chaetetid sample and  
441 stromatoporoids studied here exhibit the same pattern of microporosity and scattered  
442 distribution of dolomite (Figs. 2, 4, 8, 9), which provides a strong argument for  
443 original skeletal composition of HMC. This strengthens similar previous  
444 interpretations of the original HMC composition of stromatoporoids (e.g. Rush &  
445 Chafetz 1991; Yoo & Lee 1993) and the Buckhorn chaetetid (Seuss et al. 2014),  
446 which were based on the occurrence of dolomite alone. The alternative  
447 interpretations, of original LMC or aragonite skeletal composition, fail to explain all  
448 the observations. An original LMC composition is not consistent with the common  
449 occurrence of microporosity and finely scattered minute dolomite. Thus, the

450 interpretation by Stanley & Hardie (1998) that Palaeozoic stromatoporoids were  
451 originally LMC, and that Mg:Ca fluctuations drove the skeletal composition of  
452 dominant reef builders, is at odds with evidence presented in this study and in  
453 papers that propose a HMC composition (e.g. Rush & Chafetz 1991; Yoo & Lee  
454 1993). Furthermore, an original aragonite composition is less likely because the  
455 orthorhombic aragonite structure makes it impossible for trigonal calcite to form  
456 syntaxial overgrowths that grow in crystallographic continuity. We note the very low  
457 levels of Sr in samples studied here (Figs. 4, 8, 9). The slightly raised concentrations  
458 of strontium (400-500 ppm) observed in one Devonian stromatoporoid specimen (Da  
459 Silva et al. 2014) are not a convincing argument for an original aragonite  
460 composition; in comparison with crinoids, concentrations of up to 1700 ppm  
461 strontium have been reported for HMC plates of echinoderms (Dickson 2001a, b).  
462 Finally, despite the argument for an original HMC composition of stromatoporoids,  
463 we note that in Stearn's (2015b) discussion of stromatoporoid mineralogy, he  
464 reported earlier studies where stromatoporoids did not contain dolomite. Thus, the  
465 link between occurrence of microdolomite inclusions and original HMC mineralogy of  
466 stromatoporoids, remains a hypothesis for which there is strong support but not  
467 proof.

468 Although this study focussed on only a few specimens, our results are  
469 consistent with the unusual preservation of Palaeozoic stromatoporoids  
470 characterised by coarse calcite crystals oriented normal to, and cutting across,  
471 horizontal galleries and vertical pillars (Kershaw 2013). As argued above, this  
472 preservation is inconsistent with an original aragonite composition. However, not all  
473 Palaeozoic stromatoporoids are preserved in this way. Semeniuk (1971), for  
474 example, described an Ordovician stromatoporoid, *Alleynodictyon*, which is  
475 preserved as a mouldic secondary calcite infill and thus might have been composed  
476 originally of aragonite. Mallamo and Stearn (1991) also interpreted aragonite for  
477 Ordovician stromatoporoids. Thus the interpretation here that Palaeozoic  
478 stromatoporoids had an original HMC composition may not apply to all of them.

479

#### 480 *Stromatoporoid mineralogy and the calcite-aragonite seas debate*

481 Here we assess the relationship between stromatoporoid mineralogy and another  
482 aspect of the aragonite-calcite seas debate, that of temperature control on  
483 mineralisation. Because Mg<sup>2+</sup> ions act as calcite-specific growth inhibitors, an  
484 increasing Mg:Ca ratio favours the precipitation of aragonite in non-biogenic settings  
485 (Morse et al. 2007). Phanerozoic oscillations in the Mg:Ca ratio broadly coincide with  
486 the original mineralogy of non-biogenic CaCO<sub>3</sub> precipitates and the composition of  
487 evaporites throughout the Phanerozoic (Sandberg 1983; Hardie 1996) and have thus  
488 been widely regarded as the main drivers of Phanerozoic aragonite-calcite sea  
489 conditions. However, experimental work has shown that whether non-biogenic  
490 CaCO<sub>3</sub> precipitation results in aragonite or calcite is strongly temperature dependent  
491 (Morse et al. 1997; Balthasar & Cusack 2015). Throughout the Phanerozoic Eon, this  
492 temperature effect on CaCO<sub>3</sub> polymorphs should have resulted in a much higher  
493 proportion of non-biogenic aragonite precipitation in shallow tropical seas than  
494 proposed from the traditional focus on the Mg:Ca ratio alone (Balthasar & Cusack  
495 2015). Following Eichenseer et al. (2019), we combined the relationships between  
496 temperature, Mg:Ca ratio and the percentage of aragonite as described by Balthasar  
497 and Cusack (2015), with δ<sup>18</sup>O-based tropical shallow-water temperature estimates  
498 (Veizer & Prokoph 2015) and the Mg:Ca ratios modelled by Demicco et al. (2005) to  
499 create a measure of 'aragonite sea intensity' through time. We thus argue that non-

500 biogenic aragonite was likely to have fluctuated substantially throughout the  
501 Palaeozoic (Fig. 13). Particularly through the Ordovician-Devonian period this  
502 fluctuation was mainly driven by temperature as the Mg:Ca ratios remained at or  
503 slightly below 1 (Fig. 13).

504 Considering that, throughout their mid-Ordovician to Early Carboniferous  
505 stratigraphic range (Kershaw & Sendino 2020), the skeletal composition of  
506 Palaeozoic stromatoporoids is interpreted here to have been mainly HMC, it seems  
507 unlikely that temperature significantly influenced their skeletal mineralogy. In addition  
508 to stromatoporoids, it is useful to assess the skeletal composition of entire  
509 stromatoporoid-dominated reefs. To do this we considered sponge-dominated reefs  
510 in the PaleoReefs Database (PARED) (Fig. 13). The reef mineralogy in PARED is  
511 estimated based on the original mineralogy of the main reef builders of each  
512 individual reef (Kiessling et al. 2008) and thus shows that stromatoporoids were  
513 mainly associated with other calcitic reef builders in sponge-dominated Ordovician –  
514 Devonian reefs. The minor contributions of likely aragonitic organisms in these reefs  
515 are mainly due to fossils such as *Tetradium* and receptaculitids. Following the late  
516 Devonian mass extinction, sponge-dominated reefs were rare until the Late Permian  
517 but, where they are recorded, they are interpreted as having been dominated by  
518 originally aragonitic reef builders (Fig. 13).

519 Together, the data discussed above are presented as evidence that, contrary  
520 to the effect of temperature on non-biogenic CaCO<sub>3</sub> polymorph formation, the  
521 skeletal composition of Palaeozoic stromatoporoids was not noticeably influenced by  
522 temperature. The Mg:Ca ratio, on the other hand, shows a reasonably good  
523 correlation with the skeletal composition of stromatoporoids and with the mineral  
524 composition of Palaeozoic reefs dominated by hypercalcified sponges. It thus  
525 appears that the skeletal composition of Palaeozoic hypercalcifying sponges is  
526 influenced primarily by the Mg:Ca ratio instead of a combination of Mg:Ca ratio and  
527 temperature.

528 Finally we consider a caveat regarding the possible impact of biotic effects on  
529 sponge mineralisation separate from changes in global seawater. The above  
530 discussion is based on the notion that the Palaeozoic hypercalcified sponges  
531 precipitated calcium carbonate in equilibrium with contemporary seawater. However,  
532 Gaffey (1991, 1995) working on a range of living calcified organisms not including  
533 sponges, noted that because calcium carbonate skeletons are secreted within soft  
534 tissue, there is a barrier between skeleton formation sites and the external  
535 environment. This barrier breaks down when soft tissue decays and the skeletons  
536 come into contact with seawater, so the potential for very early diagenetic change to  
537 shift skeletal compositions is noted in modern organisms (Gaffey 1991). More recent  
538 work by Germer et al. (2015) and Garate et al. (2017) on non-hypercalcified  
539 sponges, identified bacterial control on precipitation of calcium carbonate spherules.  
540 The possible extent to which biological control of calcification can apply to  
541 Palaeozoic stromatoporoids and chaetetids cannot be assessed in this study, but  
542 may play a part in the reason why some stromatoporoid taxa produce a different  
543 skeletal structure from others (compare *Petridiostoma* and *Pachystroma* that occur  
544 together, discussed above). Thus, in conclusion, although we regard the Mg:Ca ratio  
545 was a key control on mineralogy of chaetetids and stromatoporoids, vital effects  
546 cannot be excluded.

547

548

549 **Conclusions**

- 550 1. A well-preserved Carboniferous chaetetid and examples of Silurian and  
551 Devonian stromatoporoids were examined using electron backscatter  
552 diffraction (EBSD). Observed microstructures are consistent with  
553 stromatoporoid skeletons having been composed originally of bundles of  
554 calcite crystals that were subsequently altered, yet retain remnant evidence of  
555 crystal bundles in the subtle variations of crystal orientations within the altered  
556 structure.
- 557 2. Presence of microdolomite within stromatoporoid partially-preserved skeletal  
558 structures is evidence of an original high-Mg calcite composition. These  
559 results are consistent with other interpretations reported in the literature.
- 560 3. Stromatoporoids flourished during a time of stable seawater Mg:Ca ratios but  
561 significant temperature variability. The low amounts of aragonite in  
562 stromatoporoid-dominated reefs throughout the Ordovician – Devonian is  
563 interpreted to indicate that the composition of these reefs was not noticeably  
564 impacted by temperature fluctuation but is consistent with an influence of the  
565 Mg:Ca ratio on the skeletal mineralogy of these reef types.

566

### 567 **Acknowledgments**

568 We are grateful for the use of the facilities of the Imaging Spectroscopy & Analysis  
569 Centre (ISAAC), School of Geographical & Earth Sciences, University of Glasgow.  
570 We also thank Mrs Heltzel for access to her private property to access the Buckhorn  
571 Asphalt Quarry. Ronald West (Kansas) facilitated collection and processing of  
572 sample illustrated in Fig. 3A. We thank Juwan Jeon (Nanjing) and Chelsea Pederson  
573 (Bochum) for careful reviews of the manuscript.

574

### 575 **Declarations**

576 Funding: BS was supported by funding from the DFG (NU 96/10-1, 2 und SE 2283/2-  
577 1). MC gratefully acknowledges support of the Natural Environment Research  
578 Council (NE/P011063/1). ACDS Acknowledges the National Science Foundation  
579 program (FNRS) for financial support (T.0051.19). KE was supported by a doctoral  
580 studentship by the University of Plymouth.

581 **Conflicts of interest/Competing interests:** there are no conflicts or competing  
582 interests associated with this study.

583 **Code availability:** not applicable.

584 **Availability of data and material** (data transparency).

585 **Authors' contributions:** UB, MC, KE and PC did the analyses; UB, SK, ACD, MC  
586 and BS wrote the paper.

587

### 588 **References**

- 589 Aizenberg J, Lambert G, Addadi L, Weiner S (1996) Stabilization of amorphous  
590 calcium carbonate by specialized macromolecules in biological and synthetic  
591 precipitates. *Advanced Materials* 8: 222–226. DOI:  
592 10.1002/adma.19960080307
- 593 Alroy J, Aberhan M, Bottjer DJ, Foote M, Fürsich FT, Harries PJ, Hendy AJW,  
594 Holland SM, Ivany LC, Kiessling W, Kosnik MA, Marshall CR, McGowan AJ,  
595 Miller AI, Olszewski TD, Patzkowsky ME, Peters SE, Villier L, Wagner PJ,  
596 Bonuso N, Borkow PS, Brenneis B, Clapham ME, Fall LM, Ferguson CA,  
597 Hanson VL, Krug AZ, Layou KM, Leckey EH, Nürnberg S, Powers CM, Sessa,  
598 CA, Simpson C, Tomašových A, Visaggi CC (2008) Phanerozoic trends in the  
599 global diversity of marine invertebrates. *Science* 321: 97-100



600 Balthasar U, Cusack M (2015) Aragonite-calcite seas-Quantifying the gray area.  
601 Geology 43: 99-102. DOI: 10.1130/G36293.1

602 Balthasar U, Cusack M, Faryma L, Chung P, Holmer LE, Jin J, Percival IG, Popov  
603 LE (2011) Relic aragonite from Ordovician-Silurian brachiopods: Implications  
604 for the evolution of calcification. Geology, 39: 967-970. DOI: 10.1130/G32269.1

605 Cusack M, England J, Dalbeck. P, Tudhope AW, Fallick AE (2008) Electron  
606 backscatter diffraction (EBSD) as a tool for detection of coral diagenesis. Coral  
607 Reefs 27: 905-911. DOI: 10.1007/s00338-008-0414-3.

608 Cusack M (2016) Biomineral electron backscatter diffraction for palaeontology.  
609 Palaeontology 59: 171-179. DOI: 10.1111/pala.12222

610 Da Silva AC, Kershaw S, Boulvain F (2011a) Stromatoporoid palaeoecology in the  
611 Frasnian (Upper Devonian) Belgian platform, and its applications in  
612 interpretation of carbonate platform environments. Palaeontology 54: 883-905.  
613 DOI: 10.1111/j.1475-4983.2011.01037.x

614 Da Silva AC, Kershaw S, Boulvain F (2011b) Sedimentology and stromatoporoid  
615 palaeoecology of Frasnian (Upper Devonian) carbonate mounds in southern  
616 Belgium. Lethaia 44: 255-274. DOI: 10.1111/j.1502-3931.2010.00240.x

617 Da Silva AC, Kershaw S, Boulvain F, Hubert BLM, Mistiaen B, Reynolds A, Reitner J  
618 (2014) Indigenous demosponge spicules in a Late Devonian stromatoporoid  
619 basal skeleton from the Frasnian of Belgium. Lethaia 47: 365-375. DOI:  
620 10.1111/let.12064

621 Demicco RV, Lowenstein TK, Hardie LA, Spencer RJ (2005) Model of seawater  
622 composition for the Phanerozoic. Geology 33: 877-880. DOI:  
623 10.1130/G21945.1.

624 Dickson JAD (1991) Carbonate mineralogy and chemistry. pp. 284-313, In: Tucker  
625 ME and Wright VP (eds): Carbonate Sedimentology. 498 pages, Blackwell  
626 Science Ltd. Oxford. ISBN 978-0-632-01472-9

627 Dickson JAD (2001a) Transformation of echinoid Mg calcite skeletons by heating.  
628 Geochimica et Cosmochimica Acta 65: 443-454. DOI: 10.1016/S0016-  
629 7037(00)00547-0

630 Dickson JAD (2001b) Diagenesis and crystal caskets: Echinoderm Mg calcite  
631 transformation, Dry Canyon, New Mexico, USA. Journal of Sedimentary  
632 Research 71: 764-777. DOI: 10.1306/2DC40966-0E47-11D7-  
633 8643000102C1865D

634 Dickson JAD (2004) Echinoderm skeletal preservation: calcite-aragonite seas and  
635 the Mg/Ca ratio of Phanerozoic oceans. Journal of Sedimentary Research  
636 74:355-365

637 Ehrlich H, Simon P, Carrillo-Cabrera W, Bazhenov V, Botting JP, Ilan M, Ereskovsky  
638 AV, Muricy G, Worch H, Mensch A, Born R, Springer A, Kummer K, Vyalikh  
639 DV, Molodtsov, S. L., Kurek, D., Kammer, M., Paasch, S., & Brunner, E. (2010).  
640 Insights into Chemistry of Biological Materials: Newly Discovered Silica-  
641 Aragonite-Chitin Biocomposites in Demosponges. *Chemistry of Materials*, **22**,  
642 1462–1471; DOI:10.1021/cm9026607

643 Eichenseer, K, Balthasar, U, Smart, C, Stander, J, Haaga, K, Kiessling, W (2019)  
644 Jurassic shift from abiotic to biotic control on marine ecological success. Nature  
645 Geoscience 12: 638–642

646 Ehrlich H, Brunner E, Simon P, Bazhenov VV, Botting JP, Tabachnick KR, Springer  
647 A, Kummer K, Vyalikh DV, Molodtsov SL, Kurek D, Kammer M, Born R,  
648 Kovalev A, Gorb SN, Koutsoukos PG, Summers A (2011) Calcite Reinforced

649 Silica–Silica Joints in the Biocomposite Skeleton of Deep-Sea Glass Sponges.  
650 Advanced Functional Materials 21: 3473–3481. DOI: 10.1002/adfm.201100749

651 Gaffey SJ (1988) Water in skeletal carbonates. Journal of Sedimentary Petrology 58:  
652 397-414

653 Gaffey S (1991) Skeletal carbonate diversity: implications for marine diagenesis. In  
654 Bain, R.J. (Ed.). Proceedings of the Fifth Symposium on the Geology of the  
655 Bahamas. Bahamian Field Station, San Salvador, Bahamas. ISBN 0-935909-37-  
656 0

657 Gaffey SJ (1995) H<sub>2</sub>O and OH in echinoid calcite – a spectroscopic study. American  
658 Mineralogist 80: 947-959

659 Garate L, Sureda J, Agell G, Uriz, MJ (2017) Endosymbiotic calcifying bacteria  
660 across sponge species and oceans. Scientific Reports 7: 43674, DOI:  
661 10.1038/srep43674.

662 Germer J, Mann K, Wörheide G, Jackson DJ (2015) The skeleton forming proteome  
663 of an early branching metazoan: a molecular survey of the biomineralization  
664 components employed by the coralline sponge *Vaceletia* sp. PLOS One 10(11):  
665 e0140100. doi:10.1371/journal.pone.0140100.

666 Gilis M, Grauby O, Willenz P, Dubois P, Legras L, Heresanu V, Baronnet A (2011)  
667 Multi-scale mineralogical characterization of the hypercalcified sponge  
668 *Petrobiona massiliana* (Calcarea, Calcaronea). Journal of Structural Biology  
669 176: 315–329. doi:10.1016/j.jsb.2011.08.008

670 Gilis M, Baronnet A, Dubois Ph, Legras L, Grauby O, Willenz P (2012) Biologically  
671 controlled mineralization in the hypercalcified sponge *Petrobiona massiliana*  
672 (Calcarea, Calcaronea). Journal of Structural Biology 178: 279–289. DOI:  
673 10.1016/j.jsb.2012.04.004

674 Gilis M, Grauby O, Willenz P, Dubois P, Heresanu V, Baronnet A (2013)  
675 Biomineralization in living hypercalcified demosponges: Toward a shared  
676 mechanism? Journal of Structural Biology 183: 441–454. DOI:  
677 10.1016/j.jsb.2013.05.018

678 Gong YUT, Killiana CE, Olson IC, Appathuraic NP, Amasinoa AL, Martin MC, Holt  
679 LJ, Wilt FH, Gilbert PUPA (2012) Phase transitions in biogenic amorphous  
680 calcium carbonate. PNAS 109: 6088–6093. DOI: 10.1073/pnas.1118085109

681 Hardie LA (1996) Secular variation in seawater chemistry: An explanation for the  
682 coupled secular variation in the mineralogies of marine limestones and potash  
683 evaporites over the past 600 m.y. Geology 24: 279-283.

684 Jackson DJ, Thiel V, Wörheide G (2010). An evolutionary fast-track to  
685 biocalcification. Geobiology 8: 191–196; DOI: 10.1111/j.1472-  
686 4669.2010.00236.x

687 Jackson DJ, Macis L, Reitner J, Wörheide G (2011) A horizontal gene transfer  
688 supported the evolution of an early metazoan biomineralization strategy. BMC  
689 Evolutionary Biology 11: article number 238. DOI: 10.1186/1471-2148-11-238

690 Kershaw S (2013) Palaeozoic stromatoporoid futures: A discussion of their  
691 taxonomy, mineralogy and applications in palaeoecology and  
692 palaeoenvironmental analysis. Journal of Palaeogeography 2: 163-182.  
693 DOI:10.3724/SP.J.1261.2013.00024

694 Kershaw S, Sendino, C (2020) *Labechia carbonaria* Smith 1932 in the Early  
695 Carboniferous of England; affinity, palaeogeographic position and implications  
696 for the geological history of stromatoporoid-type sponges. Journal of  
697 Palaeogeography 9, <https://doi.org/10.1186/s42501-020-00077-7>

698 Kiessling W, Aberhan M, Villier L (2008) Phanerozoic trends in skeletal mineralogy  
699 driven by mass extinctions. *Nature Geoscience* 1: 527-530

700 Kiessling W, (2015) Fuzzy seas. *Geology* 43: 191-192. doi:10.1130/focus022015.1

701 Mallamo MP, Stearn CW (1991) Skeletal mineralogy of Ordovician stromatoporoids:  
702 New geochemical evidence for an aragonite skeleton. *Geological Society of*  
703 *America, Abstracts with Programs* 23: 164.

704 Manuel M, Borchiellini C, Alivon E, Boury-Esnault N (2004) Molecular phylogeny of  
705 calcareous sponges using 18S rRNA and 28S rRNA sequences. *Bolletino dei*  
706 *Musei e degli Istituti Biologici dell' Universita Genova* 68: 449–461

707 Marin F, Le Roy N, Marie B, Ramos-Silva P, Bundeleva I, Guichard N, Immel F  
708 (2014) Metazoan calcium carbonate biomineralizations: macroevolutionary  
709 trends - challenges for the coming decade. *Bulletin de la Societe Geologique*  
710 *de France* 185: 217-232

711 Mori K (1969) Stromatoporoids from the Silurian of Gotland I. Stockholm  
712 *Contributions in Geology* 19: 1-100

713 Morrow C, Cárdenas P (2015) Proposal for a revised classification of the  
714 Demospongiae (Porifera). *Frontiers in Zoology* 12: article number 7. DOI:  
715 10.1186/s12983-015-0099-8

716 Morse JW, Wang Q, Tsio MY (1997) Influences of temperature and Mg:Ca ratio on  
717 CaCO<sub>3</sub> precipitates from seawater. *Geology* 25: 85-87

718 Morse JW, Arvidson RS, Lüttge A (2007) Calcium carbonate formation and  
719 dissolution. *Chemical Reviews* 107: 342-381

720 Politi Y, Arad T, Klein E, Weiner S, Addadi L (2004) Sea urchin spine calcite forms  
721 via a transient amorphous calcium carbonate phase. *Science* 306: 1161-1164.  
722 DOI: 10.1126/science.1102289

723 Rush PF, Chafetz HS (1991) Skeletal mineralogy of Devonian stromatoporoids.  
724 *Journal of Sedimentary Petrology* 61: 364-369

725 Sandberg PA (1983) An oscillating trend in Phanerozoic non-skeletal carbonate  
726 mineralogy. *Nature* 305: 19-22

727 Sarashina I, Kunitomo Y, Iijima M, Chiba S, Endo K (2008) Preservation of the shell  
728 matrix protein dermatopontin in 1500 year old land snail fossils from the Bonin  
729 islands. *Organic Geochemistry* 39: 1742-1746. DOI:  
730 10.1016/j.orggeochem.2008.08.004

731 Semeniuk V (1971) Subaerial leaching in the limestones of the Bowan Park Group  
732 (Ordovician) of central western New South Wales. *Journal of Sedimentary*  
733 *Petrology* 41: 939-950

734 Sethmann I, Wörheide G (2008) Structure and composition of calcareous sponge  
735 spicules: A review and comparison to structurally related biominerals. *Micron*  
736 39: 209–228. DOI: 10.1016/j.micron.2007.01.006

737 Seuss B, Senowbari-Daryan B, Nützel A, Dittrich S, Neubauer J (2014) A chaetetid  
738 sponge assemblage from the Desmoinesian (Upper Moscovian) Buckhorn  
739 Asphalt Quarry Lagerstätte in Oklahoma, USA. *Rivista Italiana di Paleontologia*  
740 *e Stratigrafia* 120: 3-26

741 Seuss B, Nützel A, Mapes RH, Yancey TE (2009) Facies and fauna of the  
742 Pennsylvanian Buckhorn Asphalt Quarry deposit: a review and new data on an  
743 important Palaeozoic fossil Lagerstätte with aragonite preservation. *Facies* 55:  
744 609-645. DOI: 10.1007/s10347-009-0181-9

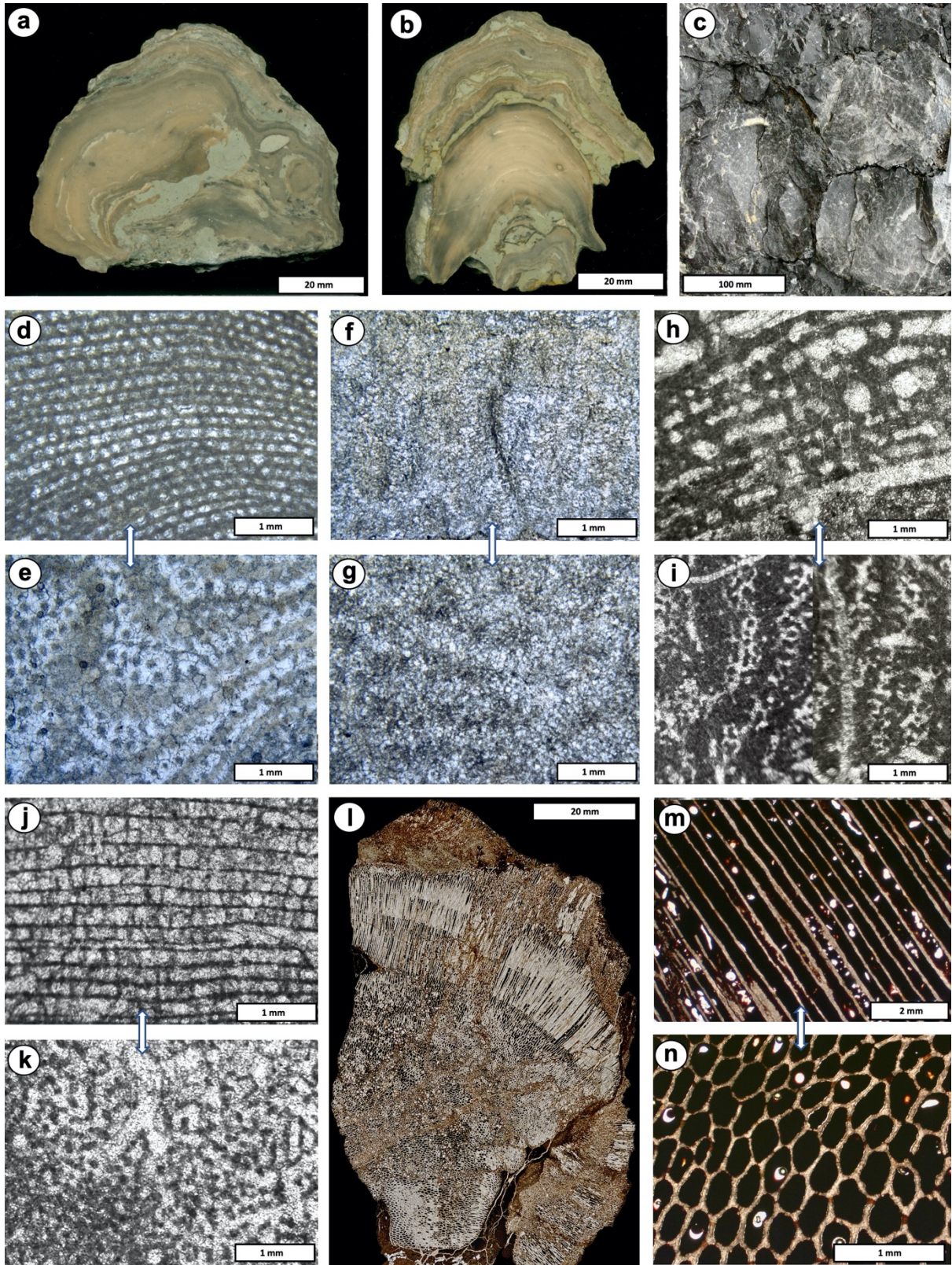
745 Smith AM, Berman J, Key MM Jr, Winter DJ (2013) Not all sponges will thrive in a  
746 high-CO<sub>2</sub> ocean: Review of the mineralogy of calcifying sponges.

- 747 Palaeogeography, Palaeoclimatology, Palaeoecology 392: 463–472. DOI:  
748 10.1016/j.palaeo.2013.10.004
- 749 Stanley SM, Hardie LA (1998) Secular oscillations in the carbonate mineralogy of  
750 reef-building and sediment-producing organisms driven by tectonically forced  
751 shifts in seawater chemistry. *Palaeogeography Palaeoclimatology*  
752 *Palaeoecology* 144: 3-19
- 753 Stearn CW (2015a) Functional morphology of the Paleozoic stromatoporoid  
754 skeleton. Pp 551-573 In Selden, P. A., ed. 2015. *Treatise on Invertebrate*  
755 *Paleontology. Part E (Revised), Porifera, vol. 4–5. The University of Kansas*  
756 *Paleontological Institute. Lawrence, Kansas. liii + 1223 p., 665 fig., 42 tables*
- 757 Stearn CW (2015b) Microstructure and mineralogy of Paleozoic Stromatoporoidea.  
758 Pp 521-542 In Selden, P. A., ed. 2015. *Treatise on Invertebrate Paleontology.*  
759 *Part E (Revised), Porifera, vol. 4–5. The University of Kansas Paleontological*  
760 *Institute. Lawrence, Kansas. liii + 1223 p., 665 fig., 42 tables*
- 761 Stearn CW, Mah AJ (1987) Skeletal microstructure of Paleozoic stromatoporoids and  
762 its mineralogical implications. *Palaios* 2: 76-84
- 763 Uriz M-J (2006) Mineral skeletogenesis in sponges. *Canadian Journal of Zoology* 84:  
764 322–356
- 765 Veizer J, Prokoph A (2015) Temperatures and oxygen isotopic composition of  
766 Phanerozoic oceans. *Earth Science Reviews* 146: 92-104. DOI:  
767 10.1016/j.earscirev.2015.03.008
- 768 Voigt O, Wülfing E, Wörheide G (2012) Molecular phylogenetic evaluation of  
769 classification and scenarios of character evolution in calcareous sponges  
770 (Porifera, Class Calcarea). *PLoS ONE* 7: 1-16, article number e33417.  
771 doi:10.1371/journal.pone.0033417
- 772 Webby, BD (2015) Glossary of terms applied to the hypercalcified Porifera. Pp 397-  
773 416 In Selden, P. A., ed. 2015. *Treatise on Invertebrate Paleontology. Part E*  
774 *(Revised), Porifera, vol. 4–5. The University of Kansas Paleontological Institute.*  
775 *Lawrence, Kansas. liii + 1223 p., 665 fig., 42 tables*
- 776 West RR (2012) Evolution of the Hypercalcified Chaetetid-Type Porifera  
777 (Demospongiae). *Treatise Online* 35:1–26
- 778 Wörheide G (1998) The reef cave dwelling ultraconservative coralline demosponge  
779 *Astrosclera willeyana* Lister 1900 from the Indo-Pacific—Morphology,  
780 ultrastructure, biocalcification, isotope record, taxonomy, biogeography,  
781 phylogeny. *Facies* 38: 1–88
- 782 Wood R (1987) Biology and revised systematics of some late Mesozoic  
783 stromatoporoids. *Special Papers in Palaeontology* 37: 1-89
- 784 Yoo CM, Lee YI, (1993) Original mineralogy of stromatoporoids. *Carbonates and*  
785 *Evaporites* 8: 224-229

786  
787  
788  
789  
790  
791

## FIGURES

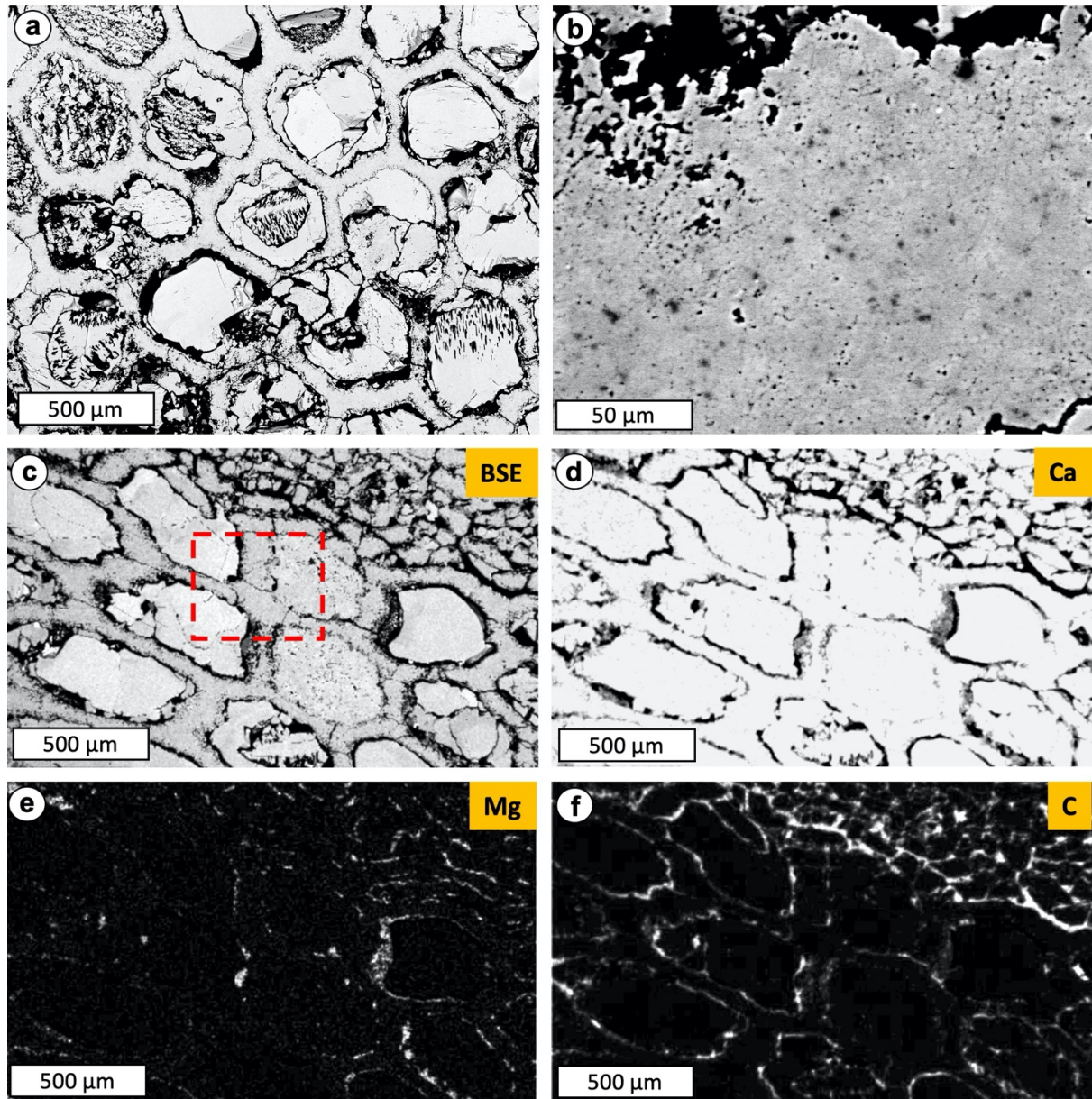




792  
 793 Fig. 1 Representative hand specimen and thin section (VS: vertical; TS: transverse)  
 794 images of stromatoporoid and chaetetid taxa used in this study. **a** and **b** Domical  
 795 stromatoporoid hand specimens in vertical section, including *Petridiostroma simplex*  
 796 and *Pachystroma hesslandi*, Upper Visby Formation, Lower Wenlock, Silurian, of  
 797 Gotland, Sweden; **c** Stromatoporoid field views in vertical section, Moulin Liénaux  
 798 Formation, middle Frasnian, Upper Devonian of La Boverie Quarry, Belgium; **d** and **e**

799 Vertical (VS, d) and transverse (TS, e) thin section views of *Petridiostroma simplex*,  
800 Gotland; **f** and **g** VS (f) and TS (g) thin section views of *Pachystroma hesslandi*,  
801 Gotland; **h** and **i** VS (h) and TS (i) thin section views of *Stictostroma*, Belgium.; **j** and  
802 **k** VS (j) and TS (k) thin section views of *Atelodictyon*, Belgium; **l** Chaetetid whole thin  
803 section from the Buckhorn Asphalt Quarry, upper Moscovian Stage, Middle  
804 Pennsylvanian, Oklahoma, USA, after Seuss et al. (2009); **m** and **n** VS(m) and TS(n)  
805 enlarged thin section views of chaetetid from Buckhorn Quarry, Oklahoma, after  
806 Seuss et al. (2009). m is sample BSPG 2011 X 20a; n and o are samples BSPG  
807 2011 X 18c stored in Bayerische Staatssammlung für Paläontologie und Geologie,  
808 Munich  
809

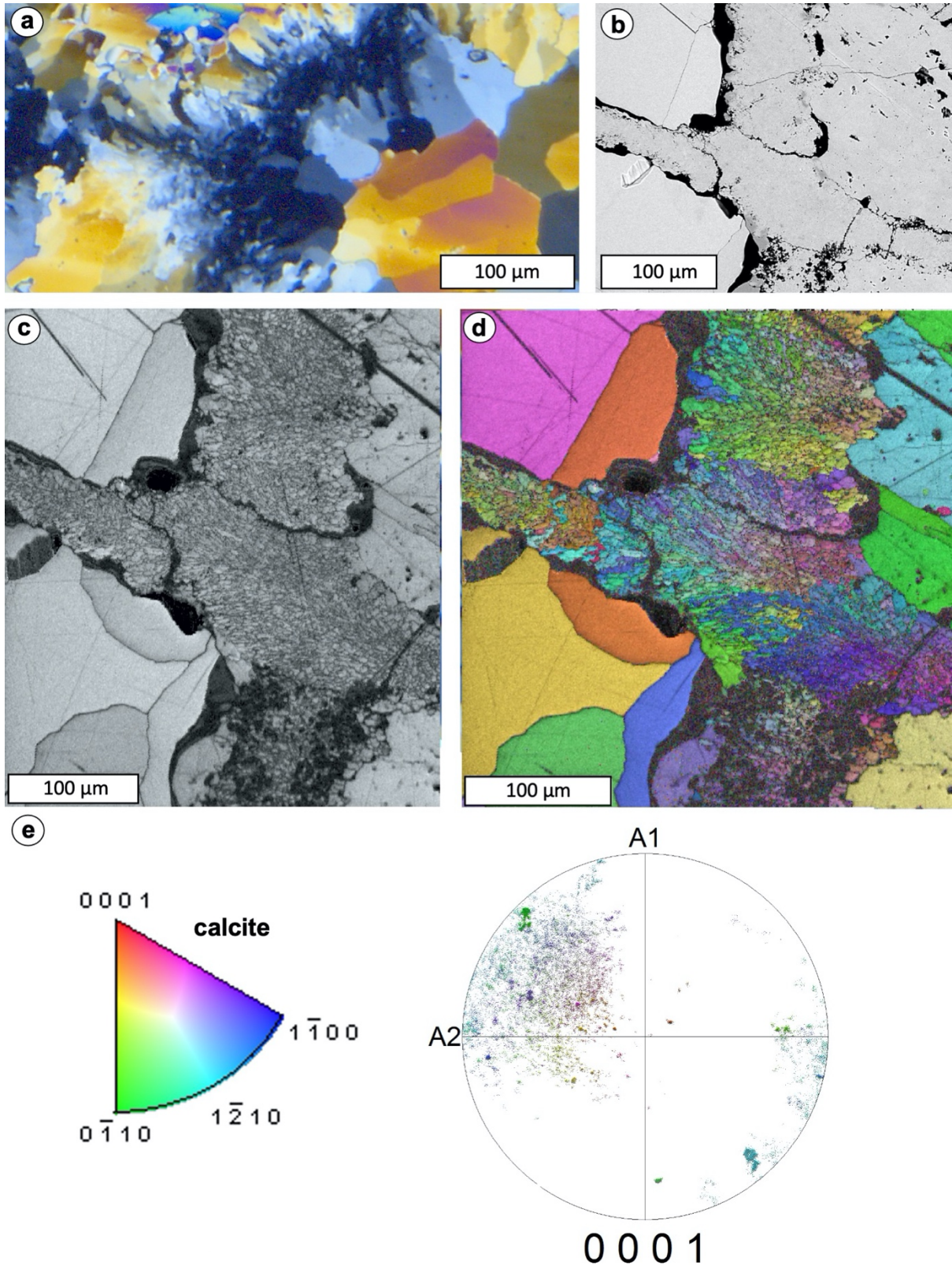




810  
 811 Fig. 2 Buckhorn chaetetid detailed structure. **a** BSE-image showing the characteristic  
 812 polygonal tubule cross sections filled with partially dissolved cements; **b** BSE close-  
 813 up of a skeletal wall showing the speckled appearance and microporosity; **c** BSE  
 814 image; red box shows the area of EBSD map shown in figure 3; **d-e** elemental maps  
 815 of Ca, Mg, and C of same area of **c**; in each case lighter tones represent higher  
 816 concentrations of each element. Note that the stretched appearance of the chaetetid

817 in c-f is because the sample is tilted to 70 degrees for EBSD scatter image  
818 acquisition, although this is an orthogonal TS view. Note this issue affects all the  
819 BSE and EBSD images in this paper  
820  
821  
822  
823

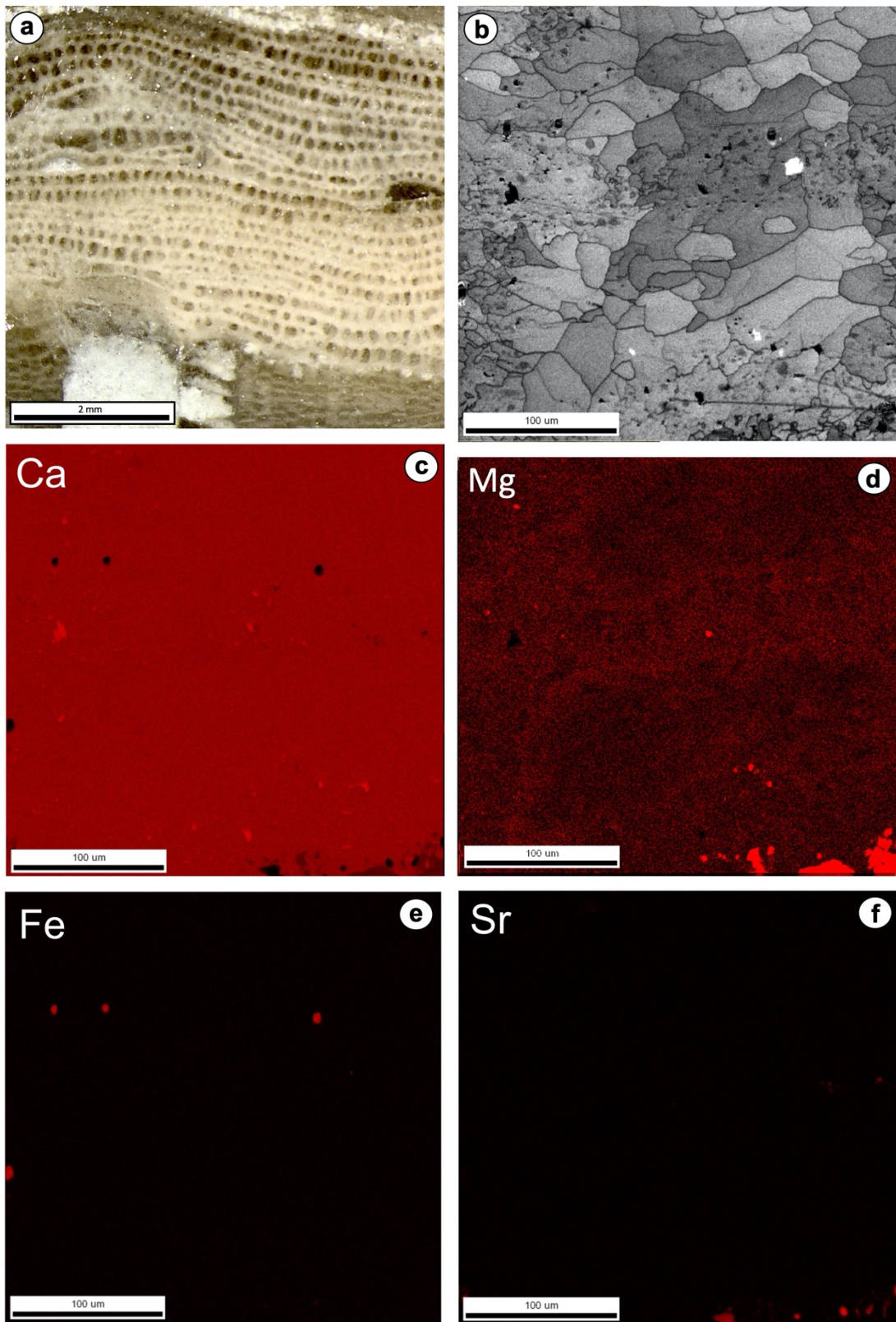




824  
 825 Fig. 3 Images of chaetetids. a Transverse ultrathin section in cross-polarised light, of  
 826 chaetetid from a quarry in the Amoret Member of Altamont Limestone Formation,  
 827 Pennsylvanian subsystem, near Coffeyville, Labette County, Kansas, showing  
 828 transverse fibrous crystal structure in the walls. Note variation of extinction in  
 829 neighbouring crystals reflecting the fibrous structure even though it is partially  
 830 altered. This sample is provided for comparison with BSE and EBSD images, in the

831 absence of similar thin sections of the Buckhorn sample. **b** BSE image, of the  
832 Buckhorn chaetetid, of the area shown in red box in Fig. 2c, showing clear distinction  
833 between calicle wall and cavity-filling sparite. Prominent major crystal boundaries in  
834 the chaetetid skeletal wall indicate overprinting by recrystallisation of its structure (for  
835 example the sharp change from purple-blue to green-yellow in the centre of the  
836 image). **c** EBSD diffraction intensity map of same area as b. This shows that  
837 variation of intensity of diffraction from different crystals within the chaetetid wall is  
838 small except in the bottom centre of the image, where the dark shades reflect low  
839 reliability of information of crystal orientation. **d** combined diffraction intensity and  
840 crystal orientation map showing good quality of orientation information across most  
841 of the image. The same is true for the cement filling the calicles. The chaetetid  
842 skeletal wall shows a sharp boundary with the calicle fill sparite, contrasting the  
843 partly recrystallised thin section view in a, in a different sample from a non-  
844 lagerstätte deposit. Compare this image with stromatoporoid EBSD images  
845 illustrated in Figs 5, 7, 10 and 11; **e** (left diagram) colour code for crystal axes in the  
846 EBSD map of d; and (right diagram) crystal orientation pole diagram, showing  
847 clustered crystal orientations consistent with a fibrous skeletal structure, discussed in  
848 the text  
849

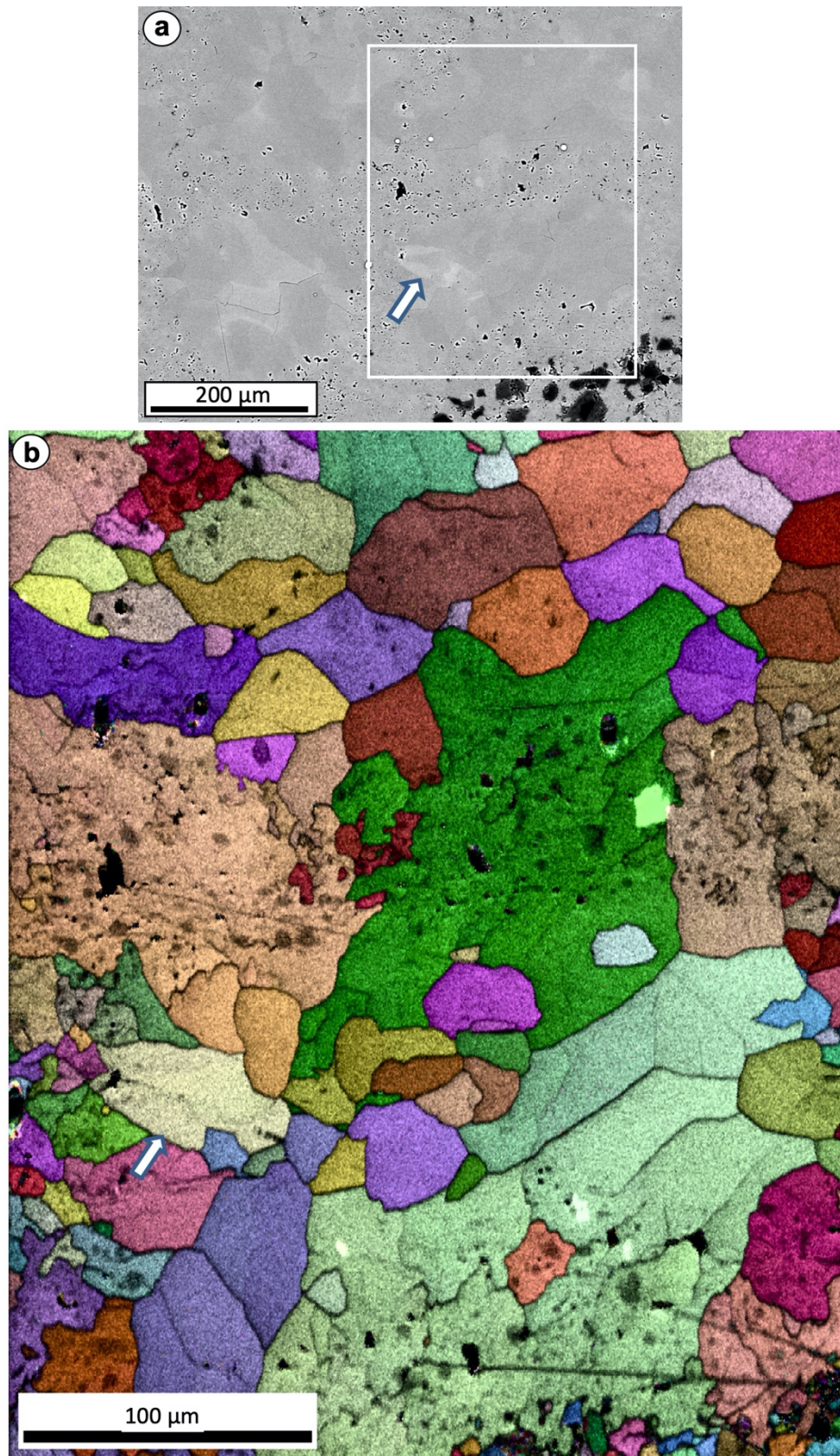




850  
 851 Fig. 4 *Petridiostroma simplex*, Silurian of Gotland, structure and elemental  
 852 composition. **a** Vertical section of hand specimen showing laminae and pillars of a  
 853 specimen that grew on top of a heliolitid tabulate after death of the tabulate,  
 854 indicated by sediment in corallites. Dark areas between laminae and pillars are  
 855 gallery spaces filled with sparite. **b** Diffraction intensity EBSD image emphasizing the  
 856 stromatoporoid skeletal structure composed of a speckled fabric overprinted by

857 diagenetic cement that passes into the gallery spaces. Two laminae (centre and  
858 bottom), most of one pillar (left) and part of another pillar (right) are illustrated, for  
859 comparison with a. The variation in grey shade between crystals corresponds to the  
860 intensity of diffraction from the sample surface; some crystals show less intensity but  
861 there is no difference in diffraction quality between the skeletal tissue and gallery  
862 cement in any crystal, likely indicating they have the same composition. **c-f**  
863 Elemental maps of the same area as b; in each case lighter tones represent higher  
864 concentrations of each element. Maps of Ca, Mg, Fe and Sr show there is very little  
865 difference between the skeletal walls and the gallery cements, typical of  
866 stromatoporoids, and discussed in the text. Levels of Sr and Fe are very low  
867





868  
 869 Fig. 5. *Petridiostroma simplex*, Gotland, skeletal structure. **a** BSE image of sample  
 870 processed in this study showing faint speckled skeletal structure contrasting the  
 871 gallery sparite. **b** Combined diffraction intensity and crystal orientation EBSD map of  
 872 the white rectangle in **a** (that also represents the area of Fig. 4b), showing colour  
 873 variation representing different orientations of calcite crystals passing between  
 874 skeleton and gallery sparite. Skeleton of stromatoporoid is clearly distinguishable

875 from the sparite cement and shows the relatively sharp edge of the skeletal  
876 structure. Diffraction intensity varies between crystals but not between the skeletal  
877 tissue and gallery cement, likely indicating similar compositions of both. White arrow  
878 in b and c mark the same location in the two images

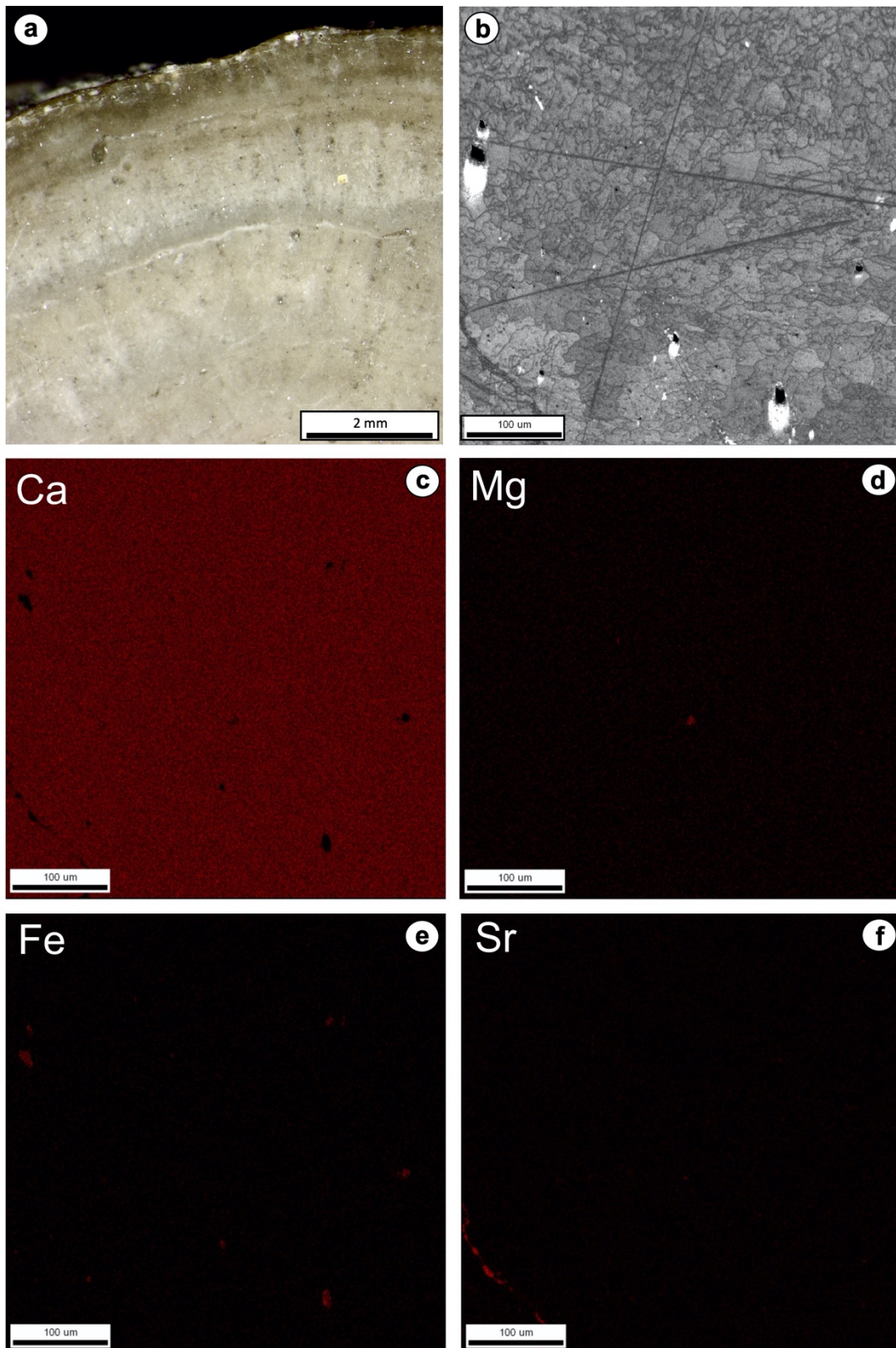
879

880

881

882

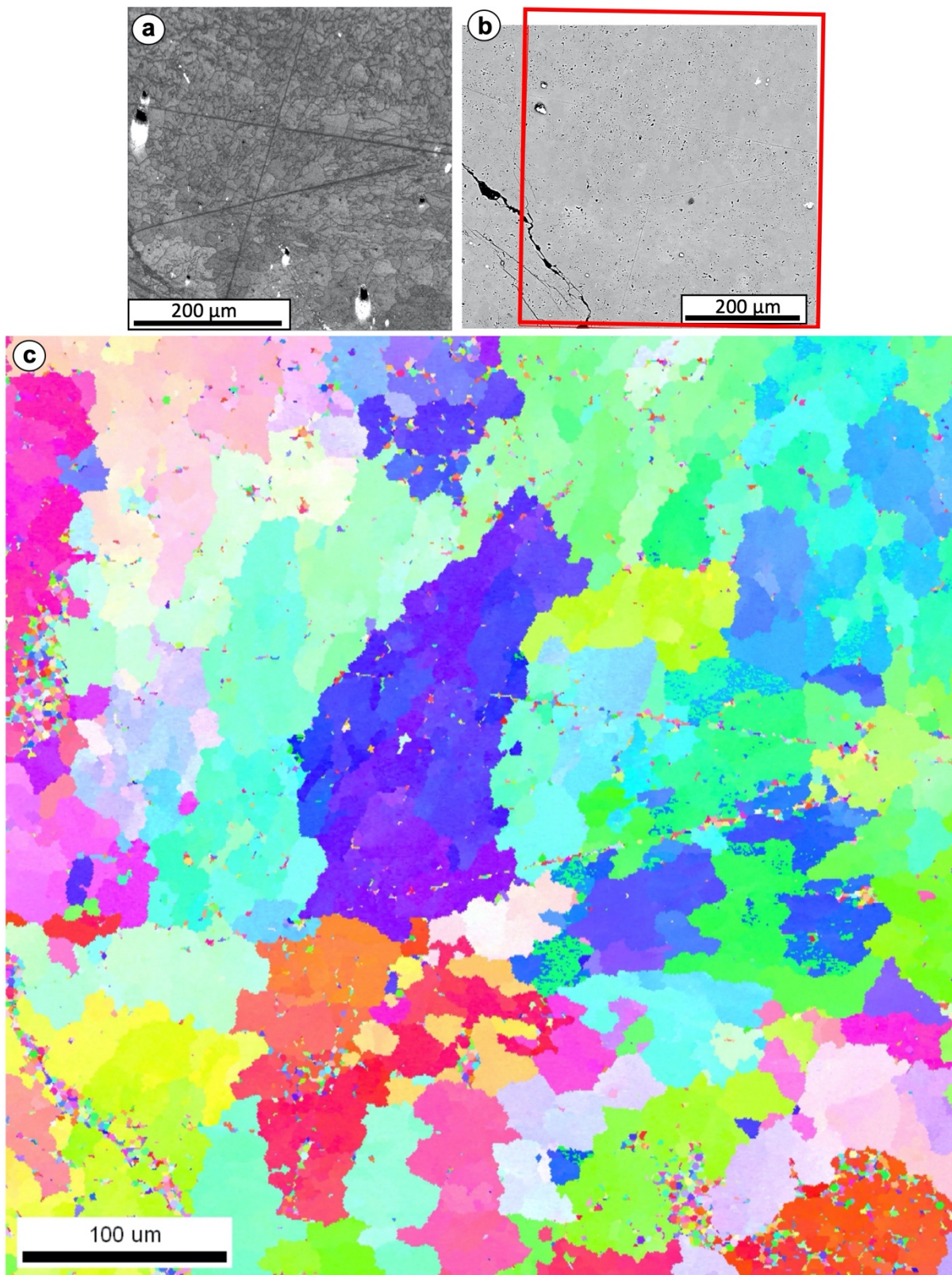




883  
 884 Fig. 6. *Pachystroma hesslandi*, Silurian of Gotland, structure and elemental  
 885 composition. **a** Vertical section of hand specimen used in this study showing  
 886 difference between the skeletal architecture of this taxon and that of *Petridiostroma*  
 887 *simplex* illustrated in Figs. 1, 4 and 5; *P. hesslandi* lacks an obvious laminae and  
 888 pillar arrangement, its skeleton being composed of a finer-structured fabric. **b**  
 889 Diffraction intensity EBSD map reflecting the fine skeletal structure so that skeletal

890 component and gallery space are not as easily recognisable in this taxon as in *P.*  
891 *simplex*. Little variation in diffraction intensity between crystals is visible indicating  
892 reliable EBSD orientation data. **c-f** Elemental maps of the same area as b; in each  
893 case lighter tones represent higher concentrations of each element. Maps of Ca, Mg,  
894 Fe and Sr may be compared with those of *P. simplex* in Fig. 4; in both taxa there is  
895 very little difference in the elemental composition between the skeleton and cements  
896 in stromatoporoids  
897

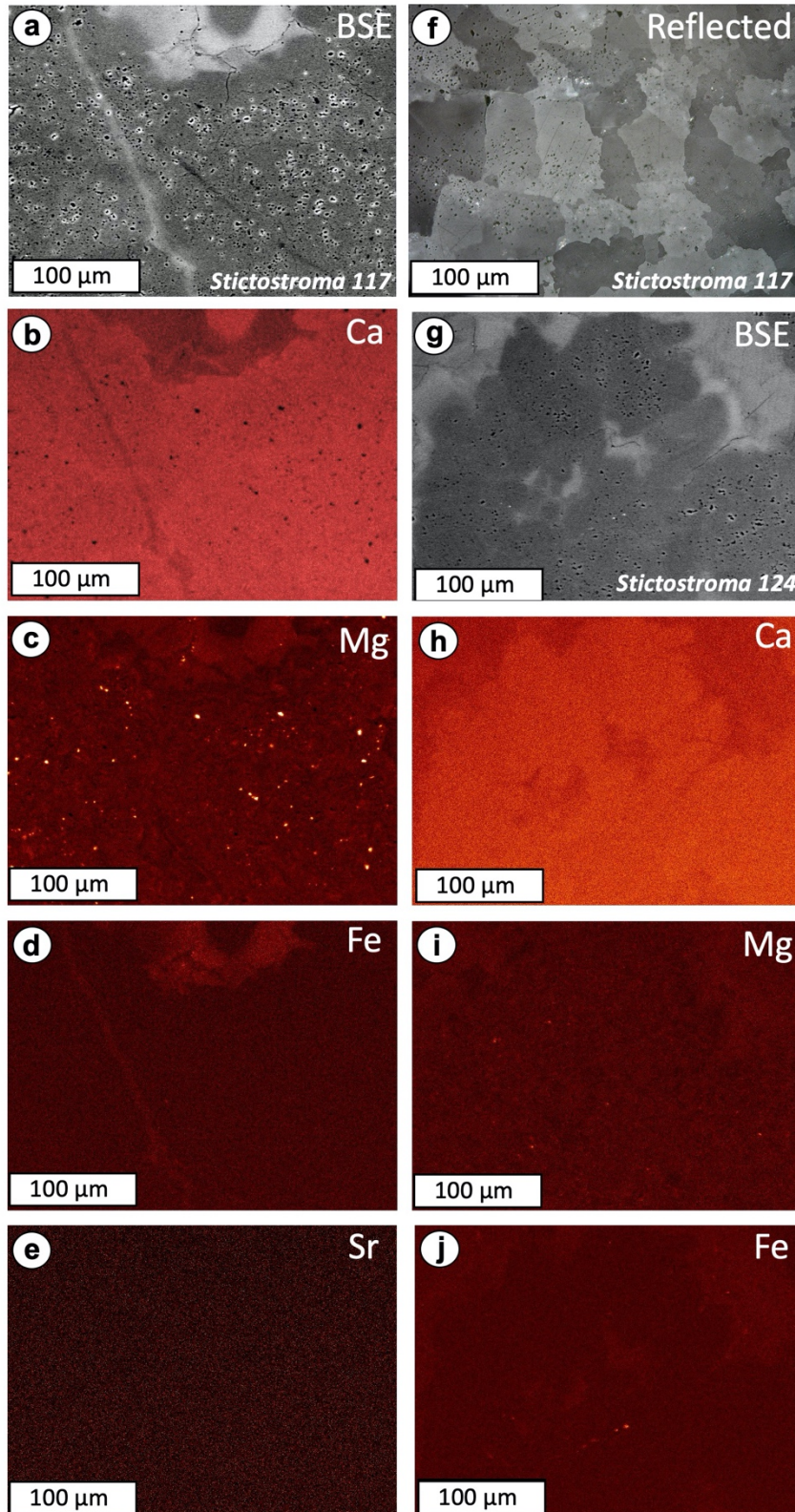




898  
 899 Fig. 7. *Pachystroma hesslandi*, Gotland, skeletal structure. **a** Repeat of diffraction  
 900 intensity EBSD map in Fig. 6b to aid understanding of the areas in Figs. 7b and c. **b**  
 901 BSE image of sample processed in this study showing the speckled skeletal  
 902 structure occurs throughout the image in contrast to *P. simplex* (Fig. 5b). Thus in this  
 903 taxon, the skeletal structure and gallery space are poorly distinguishable in b. **c**  
 904 EBSD image of the area of the red box in b and the whole area of a. Colour variation



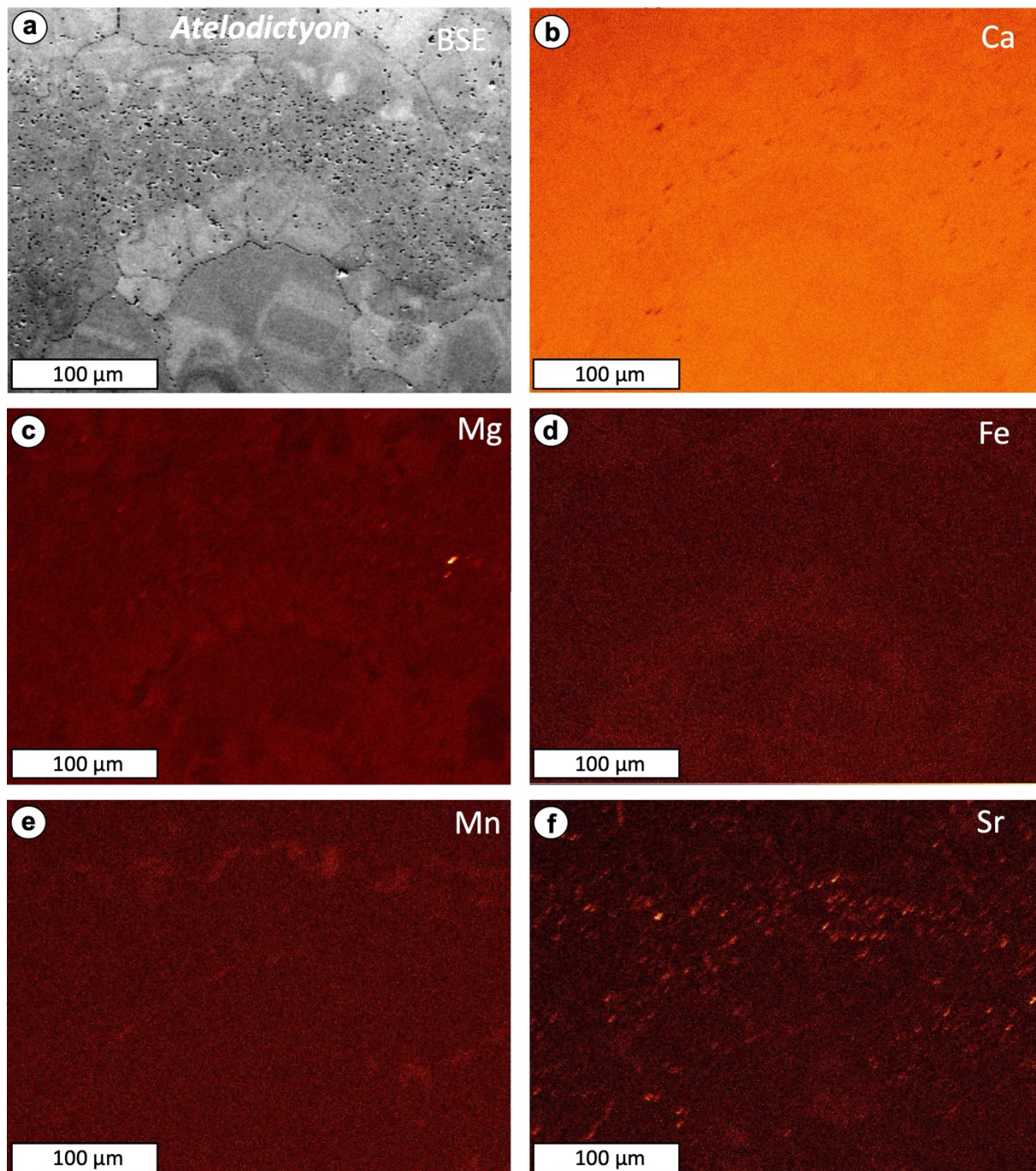
905 reflects crystal orientation. Note the contrast with *P. simplex* in Fig. 5, that has a  
906 more equant crystal structure, with less vertical elongation of crystals than in *P.*  
907 *hesslandi*. Note also the subtle colour shade changes within crystals illustrating shifts  
908 of crystal axes within the areas of larger crystals, that are interpreted to represent  
909 altered crystal bundles, discussed in the text  
910



911

912 Fig. 8. *Stictostroma*, Devonian of Belgium, structure and elemental composition in  
913 two specimens of this taxon; note that this study did not examine *Stictostroma* in  
914 EBSD. **a-e** VS views of the same area. **a** shows BSE image, highlighting margin  
915 between a lamina in the lower two thirds of the photo, and gallery space in the upper  
916 one third; bright dots are inclusions in the skeletal structure. **b-e** shows elemental  
917 maps. **f** shows a reflected light image of an area near to a-e, showing the polished  
918 surface used in this study and demonstrates the recrystallised stromatoporoid  
919 structure. **g-j** VS views of the same area (g shows the margin between a lamina in  
920 the lower one third of the photo, and gallery space in the upper two thirds). h-j are  
921 elemental maps indicated on each image; in each case lighter tones represent  
922 higher concentrations of each element. As in the Silurian samples from Gotland, the  
923 images in this figure demonstrate there is very little variation of key elemental  
924 components in *Stictostroma*  
925

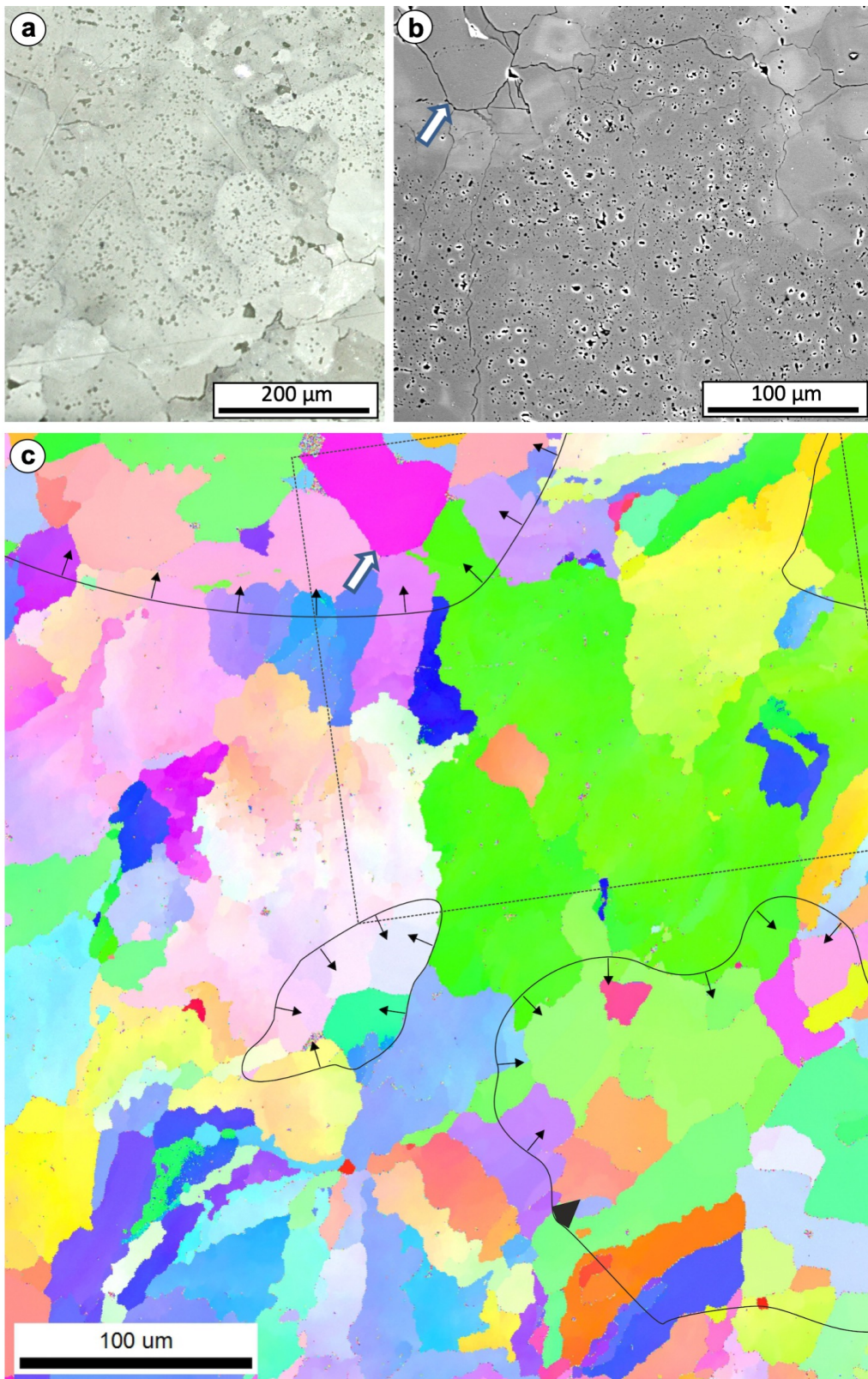




926  
 927 Fig. 9. *Atelodictyon*, Devonian of Belgium, structure and elemental composition in  
 928 one specimen of this taxon. **a** Vertical section showing BSE image with a lamina of  
 929 the stromatoporoid skeletal structure in the central one third of the picture, and  
 930 gallery space in the lower and upper parts, with prominent calcite sparite. **b-f** Vertical  
 931 section views of elemental maps indicated on each image, of the same area as **a**,  
 932 showing, as in the Silurian samples (Figs. 4 and 6) and the other Devonian sample



933 (Fig. 8), that there is little difference between key elements of the skeleton and  
934 gallery cements  
935



936  
937 Fig. 10. *Atelodictyon*, Devonian of Belgium, skeletal structure. **a** Reflected light  
938 image from the polished surface of sample used in this study. This image is from a  
939 different area from that illustrated in b and c. **b** Vertical section of BSE of part of the



940 area in c, located by the oblique rectangle in c. This image more clearly shows the  
 941 speckled appearance of the stromatoporoid skeleton contrasting the clear areas of  
 942 gallery cement. **c** EBSD colour image of same area as a, showing a general vertical  
 943 orientation of crystal structure that is typical of stromatoporoids. For the colour key,  
 944 see Fig. 3e. Curved lines with arrows highlight the skeleton margin with arrows  
 945 pointing into the gallery areas. Note the subtle colour shade changes within crystals  
 946 illustrating shifts of crystal axes within the areas of larger crystals, evidence of  
 947 altered crystal bundles, discussed in the text. White arrow marks matched points in b  
 948 and c  
 949

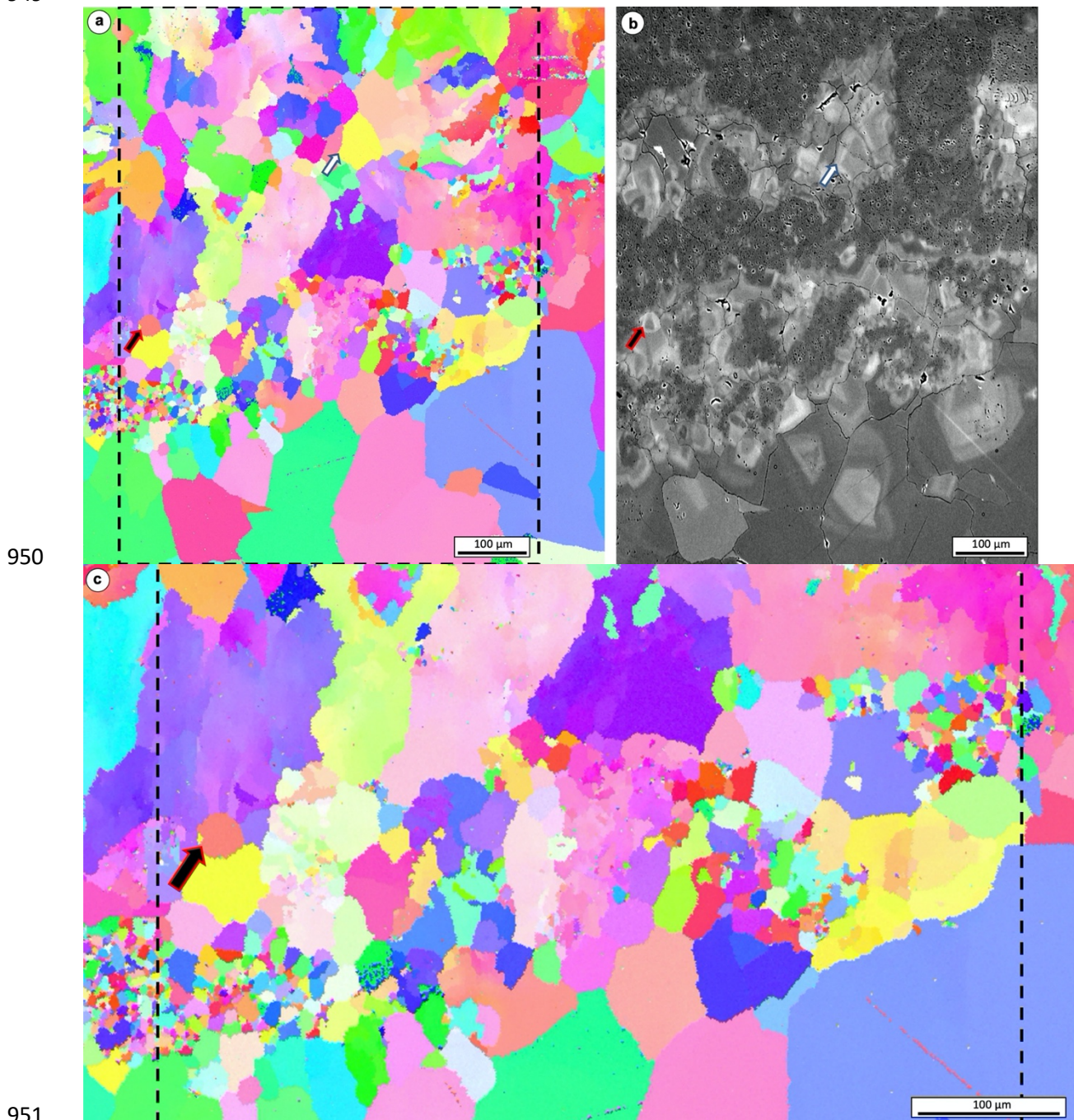
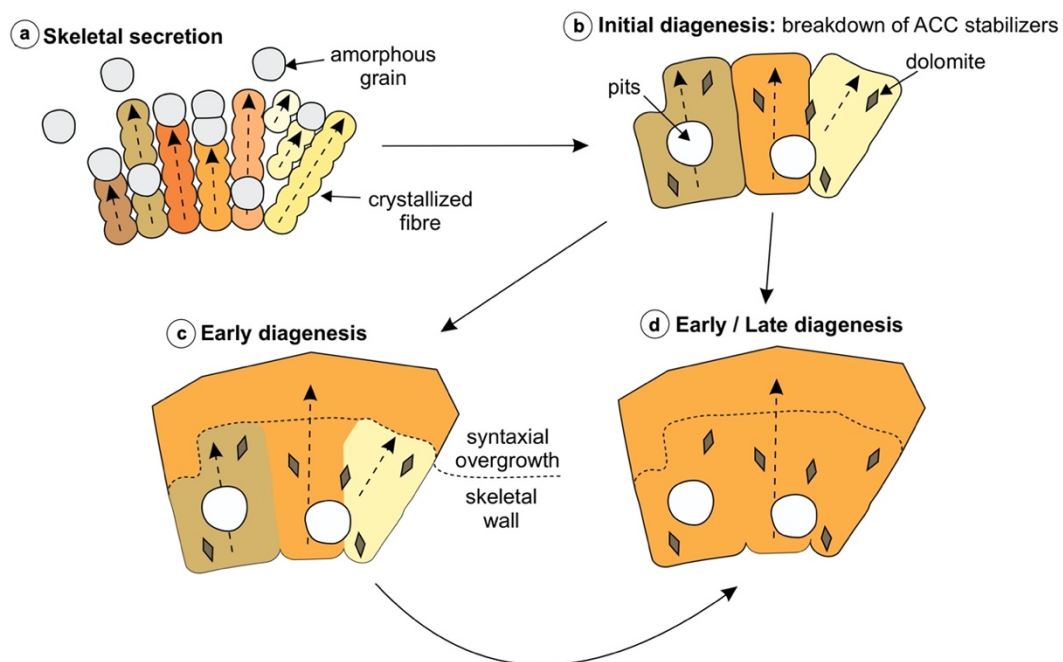


Fig. 11. *Atelodictyon*, Devonian of Belgium, skeletal structure. **a** Vertical section showing EBSD crystallographic orientation map, where the areas of smaller crystals are stromatoporoid skeleton contrasting the larger areas of gallery cement. For the

955 colour key, see Fig. 3e. As in the other images of stromatoporoids illustrated in this  
 956 study, a general vertical orientation of crystal structure is visible here. Note the subtle  
 957 colour shade changes within crystals illustrating shifts of crystal axes within the  
 958 areas of larger crystals, evidence of altered crystal bundles, discussed in the text. **b**  
 959 Vertical section of BSE map of the area of the box in a, white and black/red arrows  
 960 mark matched points in the two images. This picture very clearly shows the speckled  
 961 appearance of the stromatoporoid skeleton contrasting the clear areas of gallery  
 962 cement. **c** Enlargement of a showing the subtle shading within larger crystals in more  
 963 detail, illustrating small variations in sub-crystal orientation (e.g. the two large blue-  
 964 purple areas upper centre and upper left)

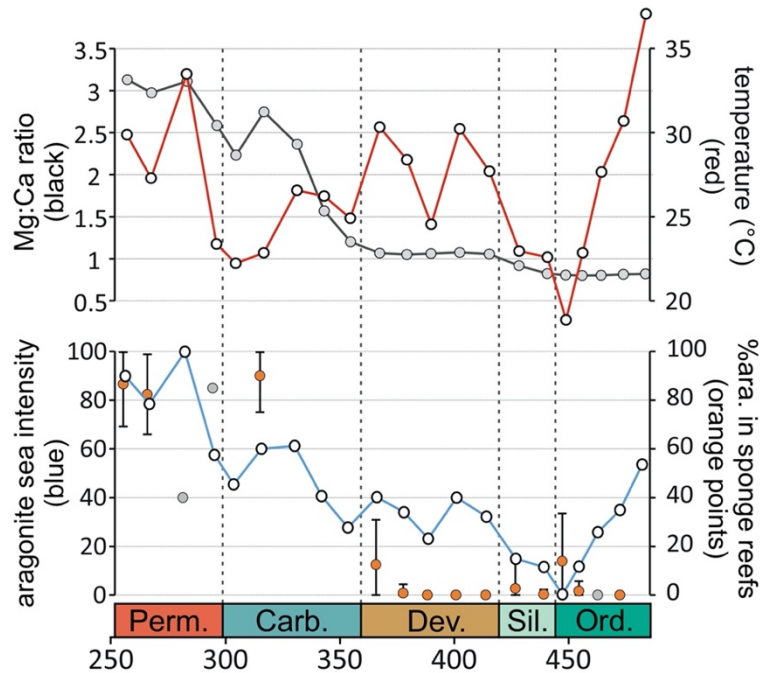
965  
 966  
 967  
 968  
 969



970  
 971 Fig. 12. Proposed diagenetic model of Palaeozoic stromatoporoid skeletons. **a** Model  
 972 of skeletal secretion (based on Gilis et al. 2011) in which amorphous grains  
 973 assemble to form fibres or aggregates. The initially 'mushy' amorphous grains  
 974 crystallise along a propagating crystallisation front. Different colours and dashed  
 975 arrows indicate different crystallographic orientations of individual crystal fibres. We  
 976 propose that some amorphous grains fail to crystallise and form amorphous  
 977 inclusions. **b** During initial diagenesis the amorphous inclusions disintegrate and  
 978 induce localised dissolution resulting in release of  $Mg^{2+}$ ,  $Ca^{2+}$ , and  $CO_3^{2-}$  ions that  
 979 will re-precipitate as calcite and dolomite in the vicinity. This process leads to the  
 980 coarsening of crystal fibres. **c** At the outer margins of the skeletal walls, syntaxial  
 981 overgrowth results in further enlargement of calcite crystals that now extend beyond  
 982 the skeleton into the galleries. Crystallographically similar adjacent domains will  
 983 retain their crystallographic orientation. **d** Blocky calcite crystals with micropores,  
 984 dolomite inclusions, and a syntaxial overgrowth. This could form either directly from  
 985 initial diagenesis as illustrated in b by higher dissolution and the associated growth of  
 986 one crystal at the expense of others, or by the transformation of a crystal with

987 diagenetically less stable domains of different crystallographic orientation (as shown  
 988 in c) into a crystallographically homogenous single crystal

989  
 990  
 991  
 992  
 993  
 994



995  
 996 Figure 13. Aragonite-Calcite sea conditions and mineral composition of sponge-  
 997 dominated Palaeozoic reefs. Upper chart shows Mg:Ca ratio (Demichco et al. 2005)  
 998 and temperature estimate (Veizer & Prokhov 2015) for 21 Palaeozoic time bins.  
 999 Lower chart shows combined effect of Mg:Ca ratio and temperature on non-biogenic  
 1000 CaCO<sub>3</sub> polymorph precipitation (based on Eichenseer et al. 2019); Orange and grey  
 1001 dots: average mineral composition of 341 sponge-dominated Palaeozoic reefs as  
 1002 found in the PARED. Orange dots = 5 or more reefs in bin, grey dots = 1-2 reefs in  
 1003 bin; error bars = 1 standard deviation.  
 1004